nature microbiology

Article

https://doi.org/10.1038/s41564-024-01841-4

Metabolic rearrangement enables adaptation of microbial growth rate to temperature shifts

Received: 19 September 2023

Accepted: 26 September 2024

Published online: 13 December 2024

Check for updates

Benjamin D. Knapp[1], Lisa Willis[2], Carlos Gonzalez[3], Harsh Vashistha[4], Joanna Jammal-Touma[4], Mikhail Tikhonov[5], Jeffrey Ram[6], Hanna Salman[4], Josh E. Elias[7] & Kerwyn Casey Huang[1,2,7,8]

Temperature is a key determinant of microbial behaviour and survival in the environment and within hosts. At intermediate temperatures, growth rate varies according to the Arrhenius law of thermodynamics, which describes the effect of temperature on the rate of a chemical reaction. However, the mechanistic basis for this behaviour remains unclear. Here we use single-cell microscopy to show that *Escherichia coli* exhibits a gradual response to temperature upshifts with a timescale of ~1.5 doublings at the higher temperature. The response was largely independent of initial or final temperature and nutrient source. Proteomic and genomic approaches demonstrated that adaptation to temperature is independent of transcriptional, translational or membrane fluidity changes. Instead, an autocatalytic enzyme network model incorporating temperature-sensitive Michaelis–Menten kinetics recapitulates all temperature-shift dynamics through metabolome rearrangement, resulting in a transient temperature memory. The model successfully predicts alterations in the temperature response across nutrient conditions, diverse *E. coli* strains from hosts with different body temperatures, soil-dwelling *Bacillus subtilis* and fission yeast. In sum, our model provides a mechanistic framework for Arrhenius-dependent growth.

While growth is critically dependent on the environmental temperature, microbes are unable to regulate intracellular temperature. Enteric bacteria face temperature changes across minute to hour or day timescales when colonizing hosts, while environmental species are exposed to daily and seasonal fluctuations. Despite these fundamental connections, the mechanistic underpinnings of how temperature affects microbial behaviour remain unclear.

Most studies on the cellular effects of temperature have focused on the regulatory systems that enable survival under heat and cold stress, during which molecular chaperones assist in the folding and unfolding of proteins and RNA[1,2]. While growth rate decreases at extreme, stress-response-inducing temperatures[3], there is typically a temperature range over which growth rate increases with temperature in approximate agreement with the Arrhenius Law of equilibrium thermodynamics[4,5]. The Arrhenius Law is an equation that describes the impact of temperature on the rate k of a chemical reaction ($\ln k \propto 1/T$), wherein the natural logarithm of growth rate depends approximately linearly on the inverse of the absolute temperature, with a negative slope that can be interpreted

[1]Biophysics Program, Stanford University, Stanford, CA, USA. [2]Department of Bioengineering, Stanford University, Stanford, CA, USA. [3]Department of Chemical and Systems Biology, Stanford University School of Medicine, Stanford, CA, USA. [4]Department of Physics and Astronomy, University of Pittsburgh, Pittsburgh, PA, USA. [5]Department of Physics, Washington University in St Louis, St Louis, MO, USA. [6]Department of Physiology, Wayne State University, Detroit, MI, USA. [7]Chan Zuckerberg Biohub, San Francisco, CA, USA. [8]Department of Microbiology and Immunology, Stanford University School of Medicine, Stanford, CA, USA. e-mail: kchuang@stanford.edu

as an activation energy for growth (E_a, equivalent to the barrier for enzyme kinetics)[6]. This temperature-dependent behaviour is highly conserved across diverse bacteria, archaea, yeast and mammalian cells[6], with each species exhibiting its own Arrhenius range of optimal growth temperatures and activation energy.

While theoretical work has suggested that proteome stability sets the upper bound for the growth rate of a given bacterial species across temperatures[7], there is no correlation between permissible (optimal) growth temperatures and E_a across bacteria[4], indicating that E_a is probably influenced by factors other than proteome stability. In *Escherichia coli*, the Arrhenius range is between 23 °C and 37 °C and E_a is ~13 kcal mol^{-1} (refs. 5,7), similar to the free energy released from ATP hydrolysis (12–16 kcal mol^{-1})[8], suggesting that there may be a single rate-limiting enzyme for growth. On the other hand, theoretical work on cyclical enzyme networks has suggested that E_a arises from the average activation energies over all reactions within the network[9,10], as the E_a for most biological enzymes is constrained between 5–20 kcal mol^{-1} (refs. 6,11,12). However, the factor(s) that limit growth across Arrhenius temperatures and determine E_a for a given species remain unknown.

Most previous studies of growth in the Arrhenius range have focused on steady-state growth. An early study of 133 proteins in *E. coli* showed that the concentration of most proteins was maintained across Arrhenius temperatures, suggesting that the proteome may be largely temperature insensitive[5]. However, other studies found transient changes in the synthesis of transfer (t)RNA synthetases after temperature increases[13], and a decrease from 37 °C to 28 °C resulted in significant changes to ~9% of the *E. coli* transcriptome[14], indicating a role for other environmental variables[15]. A few studies have examined growth rate response to temperature shifts; *E. coli* growth rate was shown to respond almost immediately upon temperature shifts within the Arrhenius range[13,16], while others report much longer timescales that scale with the final temperature[17].

Many factors could determine the timescale of temperature adaptation. *E. coli* cells tightly maintain membrane fluidity across all growth-permissible temperatures by regulating membrane composition[18]. Increased membrane fluidity allows for higher respiratory metabolic rates[19], but how fluidity impacts growth rate during temperature shifts is unknown. Growth rate across nutrients correlates with ribosome concentration, which is optimized through competition between protein and autocatalytic ribosome synthesis[20,21]. As a result, many models of growth focus on translation as a key growth-limiting factor[22]. However, this framework is likely inappropriate for understanding growth rate variations across temperatures, as ribosome concentration is constant across Arrhenius temperatures[5,23].

Here we demonstrate that *E. coli* cells exhibit an asymmetric growth-rate response to temperature shifts within the Arrhenius range and that these responses do not result from proteome or membrane reconfiguration, or from transcriptional regulation. We develop an autocatalytic enzyme network model that incorporates temperature-sensitive Michaelis–Menten kinetics into chained reactions. The model quantitatively captures temperature upshift and downshift responses, the effects of carbon source-dependent changes in activation energy and changes in substrate availability. These findings suggest that metabolome rearrangement largely drives the adaptation of growth rate to temperature shifts. This behaviour was conserved across diverse *Escherichia* strains and the Gram-positive *Bacillus subtilis*. The model also captured the distinct response of the fission yeast *Schizosaccharomyces pombe*, reflecting the conserved nature of metabolome rearrangement in facilitating growth adaptation to different temperatures.

Results

Steady-state growth rate determines temperature upshift response

To determine temperature sensitivity across strains of a single species, we measured the growth of 12 *E. coli* strains isolated from faecal samples of hosts with different body temperatures (Supplementary Table 1)[24,25]. All strains exhibited similar temperature sensitivity profiles, with Arrhenius behaviour between 27 °C and 37 °C (Extended Data Fig. 1a,b) and activation energies (10–15 kcal mol^{-1}) of growth (Extended Data Fig. 1c–e) consistent with a null model in which growth is determined by a single rate-limiting enzyme. The curves exhibit slightly nonlinear behaviour in Arrhenius plots (Extended Data Fig. 1c–e), which is predicted in some models of temperature-dependent kinetics as a result of additional factors (for example, proteome stability[7], molecular transition-state theory[26], enthalpic changes in core enzymes[27]). Single-cell growth rates correlated with bulk growth rates from liquid culture across the Arrhenius range (Fig. 1a, right, and Supplementary Fig. 1), with liquid-culture measurements exhibiting a small bias towards higher growth rates probably due to challenges in accurate optical density blank subtraction (Methods)[28]. These data suggest that the thermodynamic properties of *E. coli* growth are conserved and that host body temperature does not dictate the temperature sensitivity of enteric bacteria.

To identify the mechanisms underlying the temperature sensitivity of bacterial growth, we used single-cell tracking with a microscopy-compatible temperature controller[29]. For the null model in which growth depends on a single rate-limiting enzyme, growth rate would adapt immediately to the steady-state value dictated by the new temperature, and the response timescale would match that of the temperature shift. To test this model, we monitored the growth of single *E. coli* cells on LB agarose pads during 10 °C temperature shifts within the Arrhenius range (Methods and Supplementary Fig. 2).

A rapid downshift from 37 °C to 27 °C resulted in a rapid decrease in growth rate with a timescale quantitatively similar to that of the temperature shift (Fig. 1b and Supplementary Fig. 3), nearly reaching the steady-state growth rate at 27 °C, and then slowly decelerating towards the new steady state (Fig. 1b). In contrast, temperature upshifts from 27 °C to 37 °C resulted in a slow response, with an initial 'spike' that peaked at ~3 min post shift and subsequent linear acceleration until reaching the 37 °C steady-state growth rate at ~40 min post shift (Fig. 1c), a response time substantially longer than the doubling time at 37 °C (~22 min). To identify whether initial temperature affects the response to upshifts, we shifted *E. coli* from steady-state growth on LB at 27 °C to 30 °C, 33 °C or 37 °C. In each case, the upshift caused an initial spike and subsequent linear acceleration up to the steady-state growth rate at 37 °C (Fig. 1c,d). However, the timescale of the overall response depended on the final temperature, with longer response times observed for lower final temperatures (despite the smaller difference in steady-state growth rates between the initial and final temperature, Fig. 1d). By normalizing time t by the doubling time at the final temperature (τ_D) (Fig. 1e) and the change in growth rate to span from 0 to 1, all trajectories collapsed onto a single curve. The response time was 1.6 ± 0.2 doublings at the final temperature (Fig. 1f), even for temperatures outside the Arrhenius range (Extended Data Fig. 2) and across growth media (Fig. 1g,h), indicating that the response is largely determined by the growth rate at the elevated final temperature.

Temperature upshift responses were largely unaffected by the presence of oxygen (Extended Data Fig. 3a,b) or chaperones (Extended Data Fig. 3c–e). Under nutrient limitation, the enzymes SpoT and RelA produce the alarmone ppGpp, which signals large-scale transcriptional reprogramming known as the stringent response that regulates metabolism[30–32]. During an upshift from 27 °C to 37 °C, the response time of a Δ*spoT* Δ*relA* mutant was longer than the parent strain's (Extended Data Fig. 3f,g), and an upshift from 27 °C to 42 °C caused Δ*spoT* Δ*relA* cells to rapidly decelerate from 0.8 h^{-1} to 0.4 h^{-1} (Extended Data Fig. 3h). Thus, the impact of the stringent response on growth under temperature upshifts suggests that the response timescale is related to metabolism.

https://doi.org/10.1038/s41564-024-01841-4

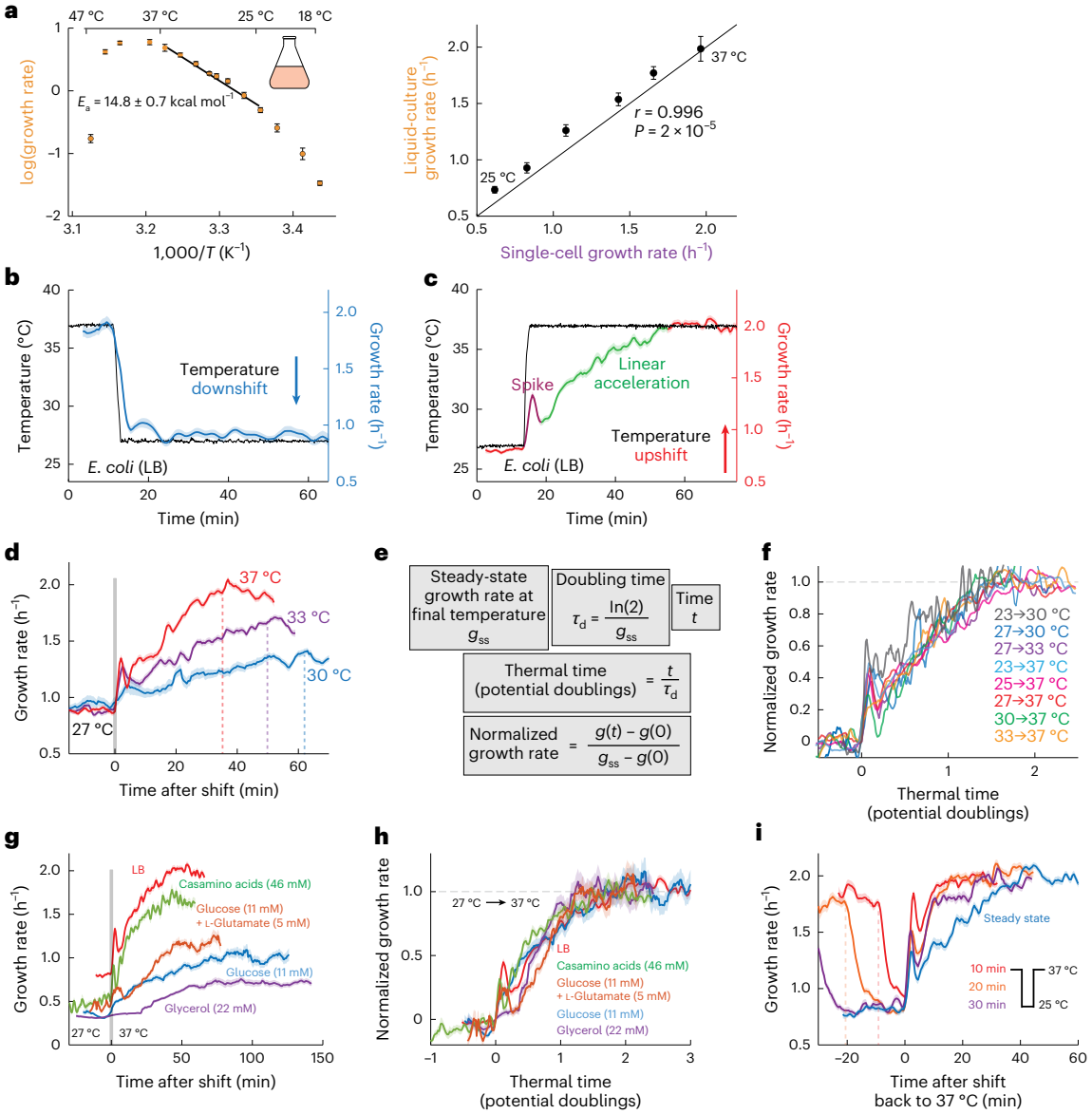

Fig. 1 | *E. coli* responds asymmetrically to temperature shifts, and upshift dynamics are determined by the steady-state growth rate at the final temperature. a, Left: Arrhenius plot illustrating that the natural logarithm of *E. coli* MG1655 maximal growth rate for temperatures between 25 °C and 37 °C varies linearly with the inverse absolute temperature, with a negative slope whose magnitude is the activation energy (E_a). Right: liquid-culture and single-cell growth rates were highly correlated for temperatures in the Arrhenius range between 25 °C and 37 °C (data from Extended Data Fig. 1c,e). Weighted linear regression was performed on growth rates between 25 °C and 37 °C, with error bars representing the 95% confidence interval of the fitted slope. **b**, Single-cell growth rate (blue) of *E. coli* MG1655 throughout a temperature (black) downshift from 37 °C to 27 °C in rich growth medium (LB) (n = 253 cells). The curve and the shaded region represent the growth rate mean ± 1 standard error of the mean (s.e.m.). Growth rate responds quickly to the downshift. **c**, Single-cell growth rate (red) of *E. coli* MG1655 throughout a temperature (black) upshift from 27 °C to 37 °C in LB (n = 792 cells). The curve and the shaded region represent the growth rate mean ± 1 s.e.m. Growth rate initially spikes (dark red), followed by linear acceleration (green) to the new steady-state value over ~35 min. **d**, Single-cell growth rate of *E. coli* MG1655 throughout a temperature upshift from 27 °C to 30 °C (blue, n = 253 cells), 33 °C (purple, n = 754 cells) or 37 °C (red, n = 904 cells) in LB. Vertical dashed lines indicate the time at which the growth rate reached its steady-state value at the higher temperature. Curves and the shaded regions represent the growth rate mean ± 1 s.e.m. **e**, The thermal time is defined as the time (t) measured in units of doubling times (τ_d) of steady-state growth at the higher temperature. The normalized growth rate is defined as the difference between the growth rate at time t ($g(t)$) and the growth rate at the temperature shift ($g(0)$) divided by the difference between the steady-state growth rate at the higher temperature (g_{ss}) and the initial temperature ($g(0)$). **f**, Normalized single-cell growth rate of *E. coli* MG1655 grown in LB exhibits a characteristic response with respect to thermal time for shifts between two temperatures in the Arrhenius range 23 °C–37 °C (n = 253–904 cells). Curves represent the mean and error bars have been omitted for ease of viewing. **g**, Single-cell growth rate of *E. coli* MG1655 throughout a temperature upshift from 27 °C to 37 °C in LB (red, n = 792 cells), casamino acids (green, n = 270 cells), glucose (blue, n = 353 cells), glucose + glutamate (orange, n = 220 cells) or glycerol (purple, n = 520 cells). Curves and the shaded regions represent the growth rate mean ± 1 s.e.m. **h**, Despite the wide variation in absolute growth-rate responses (**g**), normalized growth rate followed an approximately conserved trajectory versus thermal time across nutrient environments. **i**, Single-cell growth rates of *E. coli* MG1655 in LB grown to steady state at 37 °C and then subjected to pulses at 25 °C for 10 min (red, n = 1,015 cells), 20 min (orange, n = 1,022 cells) or 30 min (purple, n = 586 cells). Vertical dashed lines represent the times at which cells were subjected to the downshift to 25 °C for the 10- and 20-min pulses. The upshift from steady-state growth at 25 °C to 37 °C is also shown for comparison (blue, n = 773 cells). Curves and the shaded regions represent the growth rate mean ± 1 s.e.m.

https://doi.org/10.1038/s41564-024-01841-4

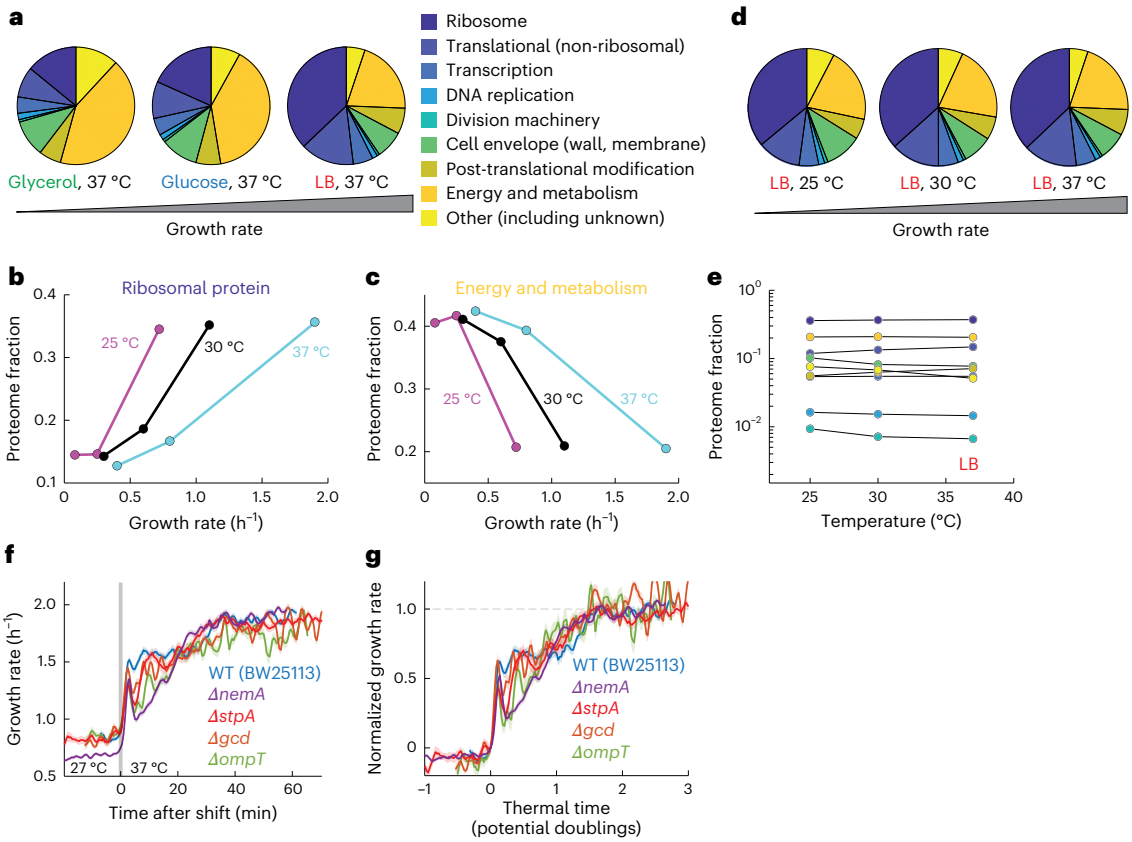

Fig. 2 | The delayed response to a temperature upshift is not due to proteome rearrangement. a, The *E. coli* proteome at 37 °C varies across media. Functional proteomic sectors (pie chart) were annotated according to the COG classification (Methods). **b**, Ribosomal protein fraction increased with growth rate across media (MOPS + glycerol, MOPS + glucose, LB), independent of growth temperature. **c**, Energy and metabolism protein fraction decreased with growth rate across media (MOPS + glycerol, MOPS + glucose, LB), independent of growth temperature. **d**, The *E. coli* proteome in LB is largely invariant across temperatures in the Arrhenius range (25 °C–37 °C). **e**, The proteome fraction accounted for by each functional category was approximately constant in LB across Arrhenius temperatures. Colours correspond to the functions in the legend in **a**. **f**, Temperature-upshift (27 °C–37 °C) responses of individual deletion mutants of the four most abundant of the proteins whose relative abundance scaled with temperature across all media conditions (blue, parent strain wild-type BW25113, $n = 710$ cells; purple, Δ*nemA*, $n = 1{,}052$ cells; red, Δ*stpA*, $n = 588$ cells; orange, Δ*gcd*, $n = 814$ cells; green, Δ*ompT*, $n = 324$ cells). Curves and shaded regions show the growth rate mean ± 1 s.e.m. **g**, Normalized growth rate followed an approximately conserved trajectory versus thermal time across the mutant growth data in **f**.

Downshift pulses reveal a temperature memory

Since adaptation to an upshift requires longer than the doubling time at the final temperature, it is likely that a component that limits growth is produced to attain the steady-state growth rate at the higher temperature. In the absence of rapid degradation, after a temperature downshift, the level of such a limiting component would represent memory of the growth state at the higher temperature until it is slowly diluted by growth down to its steady-state value at the lower temperature. To evaluate this hypothesis, we monitored *E. coli* MG1655 cells during temperature downshift pulses from 37 °C to 25 °C and back to 37 °C of varying duration. As hypothesized, after a short (10 min) interval at 25 °C, instantaneous growth rate quickly (within <10 min) recovered back to the 37 °C steady state (Fig. 1i and Extended Data Fig. 4a), accompanied by a larger spike than for cells starting from steady-state growth at 25 °C (Fig. 1i and Extended Data Fig. 4a). For the longest interval at 25 °C (30 min), the response time after the upshift back to 37 °C was still faster (~25 min, Fig. 1i and Extended Data Fig. 4a) than the steady-state response (~40 min), indicating that cells had not fully equilibrated to 25 °C. Furthermore, cells shifted back to an intermediate temperature (30 °C rather than 37 °C) after 5 min at 23 °C were able to reach the new steady-state growth rate almost immediately (Extended Data Fig. 4b). Short pulses (5–10 min) at extreme temperatures (<20 °C or >42 °C) from 37 °C generally induced rapid deceleration (Extended Data Fig. 5), but cells rapidly exited these pulses with large spike responses and re-achieved steady-state growth at 37 °C within 10–20 min (Extended Data Fig. 5b,c,e). These results suggest that a growth-limiting component is slowly diluted at the lower temperature, as cells can respond quickly to temperature fluctuations.

The *E. coli* proteome is mostly invariant across temperatures in the Arrhenius range

Within a model in which growth rate and ribosome concentration are directly coupled[22,33–35], the rapid response to temperature downshifts and the history dependence of growth rate during downshift pulses might be due to proteins limiting for growth at higher temperatures being overly abundant during the downshift, while the slow response to upshift would be due to the need for proteome reallocation[36–38]. To test this hypothesis, we performed untargeted proteomics (liquid chromatography with tandem mass spectrometry (LC–MS/MS)) on *E. coli* MG1655 during steady-state growth on three media (LB or minimal media supplemented with glucose or glycerol) at 25 °C, 30 °C and 37 °C (Fig. 2a and Supplementary Fig. 4a–c). As expected, at 37 °C the ribosomal protein fraction was positively correlated with the growth rate in each medium (Fig. 2b, light blue), while energy and metabolism fractions were negatively correlated with growth rate (Fig. 2c, light blue). However, the fraction associated with each functional group was

https://doi.org/10.1038/s41564-024-01841-4

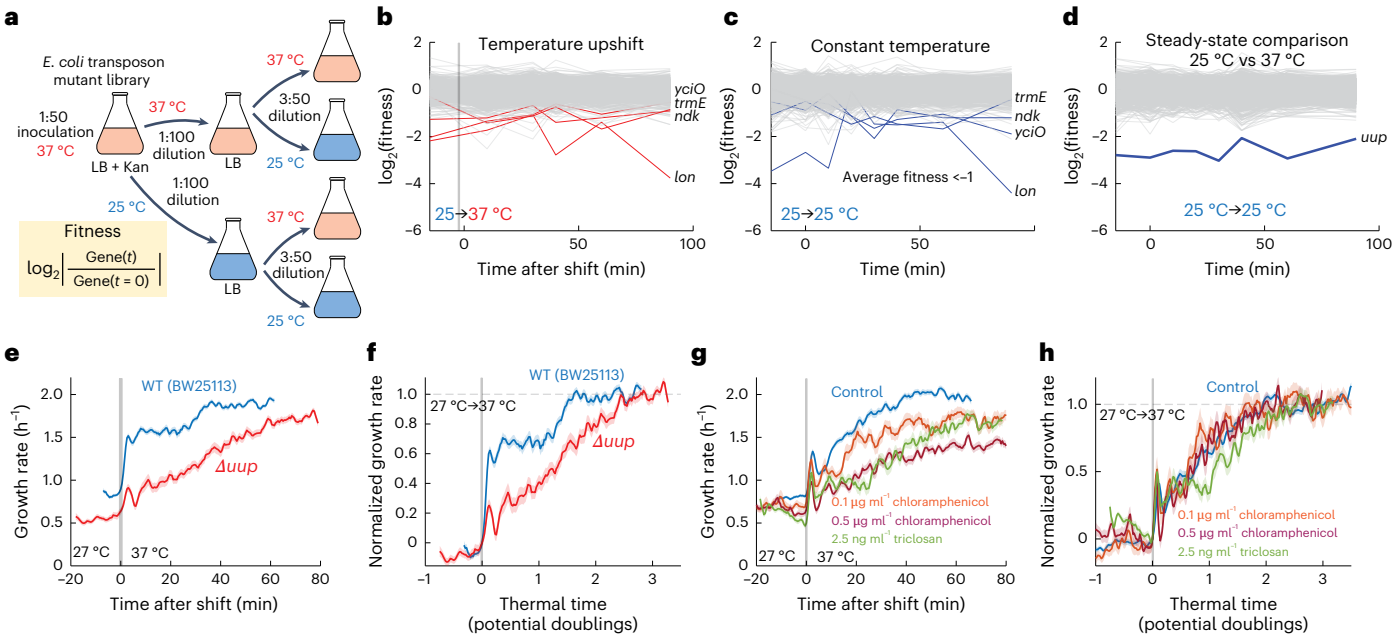

Fig. 3 | Response time is unaffected by almost all genetic and chemical perturbations. a, Schematic of temperature-shift experiments screening a pooled library of *E. coli* BW25113 randomly barcoded transposon mutants (Methods). The library was initially grown in a 50-ml volume at 37 °C, then diluted and grown to steady state at the initial target temperature (25 °C or 37 °C) before shifting to 25 °C or 37 °C at time $t = 0$. The optical density was monitored at each sampling time point (~10-min intervals). The fitness of each mutant is defined as the $\log_2$(relative abundance compared to $t = 0$) (Methods). This experiment was carried out twice. **b**, Trajectories of mutant fitness during a shift from 25 °C to 37 °C (grey vertical bar denotes timing of the shift). Mutants with fitness <−1 when averaged over time points are highlighted in red. **c**, Trajectories of mutant fitness during steady-state growth at 25 °C. Mutants with fitness <−1 when averaged over time points are highlighted in blue. **b** and **c** are from the same experiment, and outlier mutants in the upshift (**b**) were also outliers in the control (**c**). **d**, Trajectories of $\log_2$(relative abundance) during steady-state growth at 25 °C compared with those at 37 °C. A single gene, *uup*, had fitness <−1 when averaged over time points. **e**, Single-cell growth rate of Δ*uup* (red, $n = 609$ cells) and its parent BW25113 (blue, $n = 734$ cells) throughout a temperature shift from 27 °C to 37 °C. Curves and shaded regions show the growth rate mean ± 1 s.e.m. **f**, Normalized growth rate versus thermal time for each trajectory in **e** shows that Δ*uup* cells respond more slowly to an upshift. **g**, Single-cell growth rates of *E. coli* MG1655 in LB treated with 0.1 μg ml^{-1} chloramphenicol (orange, $n = 264$ cells), 0.5 μg ml^{-1} chloramphenicol (dark red, $n = 382$ cells) or 2.5 ng ml^{-1} triclosan (green, $n = 266$ cells) throughout a shift from 27 °C to 37 °C. The untreated control is also shown for comparison (blue, $n = 792$ cells). Curves and shaded regions show the growth rate mean ± 1 s.e.m. **h**, Normalized growth rate followed a similar trajectory versus thermal time as the control for the chloramphenicol treatment data in **g**, while triclosan slightly delayed the growth-rate response.

constant across Arrhenius temperatures in each medium (Fig. 2d,e and Supplementary Fig. 4d,e). We only observed notable changes for temperatures outside the Arrhenius range (16 °C, 43 °C), which is consistent with known stress-response pathways, including for the cold-shock protein CspA and major heat-shock protein DnaK (Supplementary Fig. 4d,f,g)[7,39]. Thus, ribosome fraction is unlikely to drive growth rate changes across temperatures.

Most individual protein fractions were constant across temperatures; only 13 proteins exhibited a >2-fold change between 25 °C and 37 °C independent of growth medium (Supplementary Fig. 5). The DNA-binding StpA[40] protein increased most, ~14-fold between 25 °C and 37 °C (Supplementary Fig. 5a); however, Δ*stpA* cells exhibited a similar response to a 25 °C to 37 °C upshift as wild-type cells (Fig. 2f,g), as did individual knockouts of the three next most-temperature-dependent proteins (Fig. 2f,g and Supplementary Fig. 5). Thus, the *E. coli* proteome is largely insensitive to temperature at steady state, and proteins with the largest abundance changes across Arrhenius temperatures do not impact the growth-rate response to temperature upshifts.

No single gene drives the temperature upshift response

We next explored whether specific genes drive the response to temperature shift. We performed a genome-wide, time-resolved screen using a pooled, randomly barcoded transposon mutant library in *E. coli* BW25113 (ref. 41), whereby the relative abundance of each mutant was quantified during temperature shifts between 25 °C and 37 °C (Fig. 3a and Supplementary Fig. 6a–c,f,g). No gene disruptions were consistently identified across biological replicates with a significant fitness defect specific to the temperature upshift (Fig. 3b,c and Supplementary Fig. 6c–e). The only gene of significance from our screen was *uup* (Fig. 3d and Supplementary Fig. 6g), which encodes an ABC-F protein[42]. Δ*uup* cells exhibited slight growth defects at both 27 °C and 37 °C (Fig. 3e), in contrast to other ABC-F mutants (Supplementary Fig. 6h,i), and the response time after a temperature upshift was substantially longer (~2.7 doublings versus ~1.6 for wild type) (Fig. 3f), probably due to defects in ribosome assembly[43]. Taken together, this screen suggests that none of the non-essential genes are singly responsible for the delayed growth-rate response to temperature upshifts.

To investigate the role of essential genes during temperature upshifts, we treated *E. coli* cells with a variety of antibiotics that target essential processes at sub-minimum inhibitory concentration (MIC) levels[44] and subjected them to temperature upshifts from 27 °C to 37 °C on LB (Supplementary Fig. 7). Response times remained at ~1.5 doublings for treatment with antibiotics that target the ribosome (Fig. 3g,h and Supplementary Fig. 7a,b), DNA replication and transcription, despite large impacts on growth rate in some cases (Supplementary Fig. 7c,d). Only high concentrations of fusidic acid (50 μg ml^{-1}), which disrupts translational translocation and ribosome disassembly[45], caused a significant decrease in response times (~0.2 doublings; Supplementary Fig. 7f,g). We observed similar effects in knockouts of genes responsible for tRNA modification (*tusA*, *tusB*)[46] (Supplementary Fig 7f,g), suggesting that severely impaired translational capacity under high amino acid availability causes a mismatch, allowing for fast response times.

Membrane fluidity is exquisitely regulated in *E. coli* across temperatures: the fraction of unsaturated fatty acids decreases with increasing temperature to maintain viscosity[18,19]. Triclosan, which targets membrane synthesis, increased the response time to ~2.5 doublings (Fig. 3g,h), suggesting that the delay in growth rate might be due to the need to alter membrane composition. However, disruptions to the regulation of *fabB*, which encodes the major β-ketoacyl-[acyl carrier protein] synthase responsible for elongating unsaturated fatty acids[47,48], had little effect on upshift response times, despite significant changes to membrane fluidity (Extended Data Fig. 6a–e). Increased membrane fluidity conferred a growth advantage at 37 °C (Extended Data Fig. 6f); however, it negatively affected cell growth and survival at temperatures >42 °C (Extended Data Fig. 6g,h). Thus, while membrane fluidity does not determine the timescale of upshift responses, its regulation is critical for cell integrity at high temperatures.

A temperature-sensitive enzyme network model captures response dynamics

As our proteomic, genetic and chemical screens did not uncover a key molecular regulator of the response, we developed an autocatalytic network model of growth[9,10] to interrogate alternative mechanisms.

To model growth, we incorporated three general classes of reactions: (1) import, (2) metabolite production and (3) volume expansion (Fig. 4a). Each reaction obeys Michaelis–Menten kinetics, such that metabolite c_i is consumed by enzyme e_i to produce the next metabolite c_{i+1} in the network, as in equation (1), with * representing an intermediate:

$$c_i + e_i \rightleftharpoons (c_i e_i)^* \longrightarrow c_{i+1} + e_i. \quad (1)$$

In a linear network (no branching), the dynamics of each intermediate metabolite are dictated by

$$\frac{\mathrm{d}c_i}{\mathrm{d}t} = \frac{k_{i-1}e_{i-1}c_{i-1}}{K_{i-1}+c_{i-1}} - \frac{k_i e_i c_i}{K_i + c_i} - c_i g, \quad (2)$$

where the first two terms on the right-hand side reflect enzymatic production and consumption of c_i and the last term accounts for dilution via growth at the rate g (Supplementary Text). e_i is the concentration of the ith enzyme, k_i is its catalytic rate and K_i is its Michaelis–Menten constant. Importantly, we consider the possibility that both k_i and K_i are temperature dependent with Arrhenius behaviour (Fig. 4a and Supplementary Text), consistent with experimental measurements of several enzymes[49–51]. After the final step of a reaction network of size N, an enzyme e_N consumes c_N to expand cell volume at a rate $g = \gamma_0 \frac{k_N e_N c_N}{K_N + c_N}$, where γ_0 is an efficiency factor assumed to be constant in a given environment, reflecting the conversion of c_N to a structural component of the cell envelope (Supplementary Text). From physical considerations of glucose uptake and growth rate constraints (Supplementary Text), we estimated that γ_0 is ~0.03 mM^{-1}. We refer to these equations as a temperature-sensitive enzyme network (TSEN) model.

Since the proteome is largely maintained across temperatures (Fig. 2e and Supplementary Fig. 4d), we assumed constant concentrations of each enzyme during any temperature shift. We first considered a simple model with two intermediate metabolites (minimal TSEN), identical kinetic parameters across reactions and a high (saturating) concentration of the external substrate ($c_0 \gg K_0$, Fig. 4a).

We simulated the model to reach a steady state at 27 °C and then shifted the temperature to 37 °C. The system exhibited a non-zero response time to reach the steady-state growth rate at 37 °C (Fig. 4b). The timescale for growth rate to increase by 98% of the difference between steady states was ~2 doublings (Fig. 4b), similar to our experimental observations (Fig. 1f,h). Variations in kinetic parameters largely maintained response times of 1–2 doublings (Extended Data Fig. 7a,b), as long as the E_a for the catalytic rate of the import reaction was above that of the other catalytic rates (production, growth) (Extended Data Fig. 7b). However, if the activation energy for all Michaelis–Menten constants (K_i) is 0, then the growth rate response is also immediate (Fig. 4b), highlighting the importance of temperature sensitivity of K_i. The version of the minimal TSEN without an intermediate reaction ('production-less' TSEN, Supplementary Text) is analytically tractable and predicts an upshift response time (Extended Data Fig. 7c–f) in reasonable agreement with our measurements (Fig. 1f,h). The minimal TSEN produces an Arrhenius-like growth rate (Extended Data Fig. 7g), in agreement with observations[4,6] (Fig. 1a, Supplementary Fig. 1 and Extended Data Fig. 1).

For a reaction network with N intermediates, the analytical solution of steady-state growth rate (Supplementary Text) is

$$g = \frac{\frac{k_0 e_0 c_0}{K_0 + c_0}}{\frac{1}{\gamma_0} + \sum_{i=1}^{N} c_i}, \quad (3)$$

which is set by the import rate $\frac{k_0 e_0 c_0}{K_0 + c_0}$, growth efficiency factor γ_0 (constant) and the total intracellular metabolite concentration $\sum_{i=1}^{N} c_i$. Since import changes instantaneously with temperature, the response timescale is associated with rearrangement of the metabolome. Equation (3) also reflects that growth comes at the cost of storing metabolic intermediates c_i (Supplementary Text). Many central-carbon reactions operate near their Michaelis constant K_M[52], suggesting that bottlenecks are highly likely. Within the minimal model, introducing a substrate-binding bottleneck into the production reaction characterized by a large and temperature-sensitive K_M (K_M (T = 37 °C) = 20 mM, E_a = 22.5 kcal mol^{-1}) produced strikingly physiological behaviour: an initial spike similar to our experimental observations and a response time of ~2 doublings (Fig. 4b). Moreover, when the bottleneck was embedded within a pathway involving multiple production reactions (five intermediate reactions, bottleneck in the centre), the spike broadened, and the acceleration dynamics were quantitatively similar to our experimental measurements (Fig. 4c). The TSEN model readily predicts asymmetric behaviour between upshifts and downshifts (Fig. 4d)[6]. In addition, after the initial large decrease in growth rate upon a downshift, the multiple-reaction model predicts a slow deceleration towards the slower steady-state growth rate (Fig. 4d, dark blue), similar to our experimental observations (Fig. 1b and Supplementary Fig. 3). Thus, the observed behaviours emerge from only a few simple assumptions about the network.

Since many core reactions in cells are reversible, we examined the effect of adding a single reversible (bottleneck) enzymatic reaction to the TSEN model (Supplementary Text). We found that the spike behaviour was preserved only by bottlenecking in both directions (Extended Data Fig. 8a), suggesting that such enzymes bind substrate and product similarly (that is, large and highly temperature-sensitive K_M). This finding indicates that the TSEN model's predictions of both the spike and physiological responses are compatible with reversible reactions.

Spike and response time dictated by metabolome rearrangement

In our model, metabolites after the bottleneck undergo a transient decrease in concentration after a temperature upshift (Fig. 4e) that agrees with the timescale of the spike response (Fig. 4d). This suggests that spikes are caused by rapid consumption of post-bottleneck metabolites. Meanwhile, metabolites before the bottleneck gradually build up, as do the post-bottleneck metabolites after the spike, until metabolome rearrangement has stabilized (Fig. 4e). As a result, final growth rate (which scales with temperature) dictates the thermally limited response time necessary to rearrange the metabolome. Simulations of our model captured the near invariance of the normalized

https://doi.org/10.1038/s41564-024-01841-4

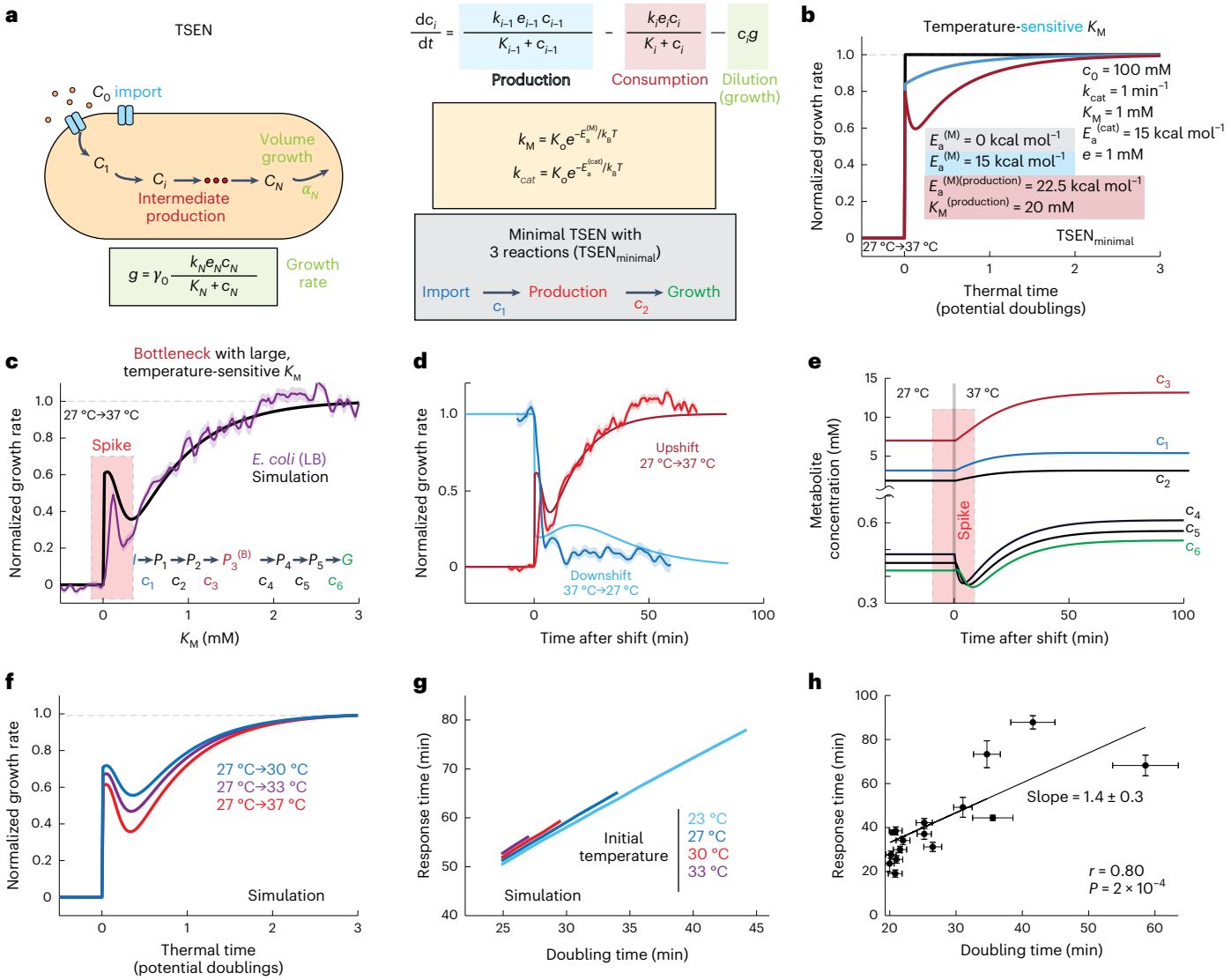

Fig. 4 | A TSEN model recapitulates temperature-shift behaviours through metabolome rearrangement. a, Left: in the TSEN model, the import reaction (blue), production reactions (dark red) and volume growth reaction (green) are chained Michaelis–Menten reactions. Right: the rate equation for each intermediate metabolite (c_i) involves enzymatic production from c_{i-1} by enzyme e_{i-1} (blue), enzymatic consumption by enzyme e_i (red) and dilution by volume growth g (green). The final intermediate c_N is translated into volume growth with an efficiency factor γ_0 (green box). Each kinetic parameter is assumed to be temperature sensitive according to an Arrhenius equation with activation energy E_a (yellow box). A minimal TSEN model ($TSEN_{minimal}$) has a single intermediate production reaction (red), such that the network has only 2 intermediate metabolites (c_1, c_2; grey box). **b**, Normalized growth rate versus thermal time from simulations of a minimal TSEN model with (blue) and without (black) a temperature-sensitive Michaelis–Menten constant (K_M) throughout a temperature shift from 27 °C to 37 °C. All other model parameters are identical and are defined in the panel inset. The TSEN with a temperature-sensitive K_M results in a non-zero response time (blue). A TSEN model with a bottleneck (dark red, K_M = 20 mM, E_a = 22.5 kcal mol^{-1}) produces an initial spike. **c**, A TSEN model with a single bottleneck (red, P_3) embedded within a 7-reaction chain produces a quantitatively similar response to an upshift from 27 °C to 37 °C as *E. coli* MG1655 cells on LB (purple, n = 792 cells; shaded region represents ±1 s.e.m.). All other reactions have parameters identical to the minimal model without a bottleneck (blue) in **b**. **d**, Normalized growth rate in simulations of the bottlenecked TSEN model in **c** throughout an upshift (dark red) or downshift (light blue) between 27 °C and 37 °C. In contrast to the spike and slow response to the upshift, the downshift results in immediate deceleration to a growth rate close to the steady-state value at 27 °C, followed by slow deceleration to a new steady-state value. Overlaid are the normalized growth rates of *E. coli* MG1655 subjected to an upshift (red, 27 °C to 37 °C, n = 792 cells) or downshift (blue, 37 °C to 27 °C, n = 253 cells). Shaded error bars represent ±1 s.e.m. **e**, The TSEN model in **c** predicts that metabolites upstream of the bottleneck ($c_{1,2,3}$) will have lower concentrations than those after the bottleneck ($c_{4,5,6}$) and increase slowly on the timescale of growth after an upshift. Post-bottleneck metabolites undergo transient decreases immediately after the temperature upshift over a time interval corresponding to the spike (red box). After this initial period, all metabolites increase to new values corresponding to the steady state at the higher temperature. **f**, The TSEN model in **c** predicts highly similar responses of normalized growth rate with thermal time for upshifts from 27 °C to 30 °C (blue), 33 °C (purple) or 37 °C (red). **g**, Over a broad range of final temperatures, the absolute upshift response time (time to reach 98% of the difference between steady-state growth rates) has linear scaling with the doubling time at the final temperature. Each line represents simulations from a given initial temperature to temperatures up to 37 °C. **h**, Experimental estimates of absolute response time follow a linear scaling with doubling time at the final temperature, similar to simulations in **g**. Shown are data for upshifts involving initial and final temperatures ranging between 23 °C and 37 °C (data from Fig. 1f–h). Weighted linear regression was performed, with error bars representing the 95% confidence interval of the fitted slope.

https://doi.org/10.1038/s41564-024-01841-4

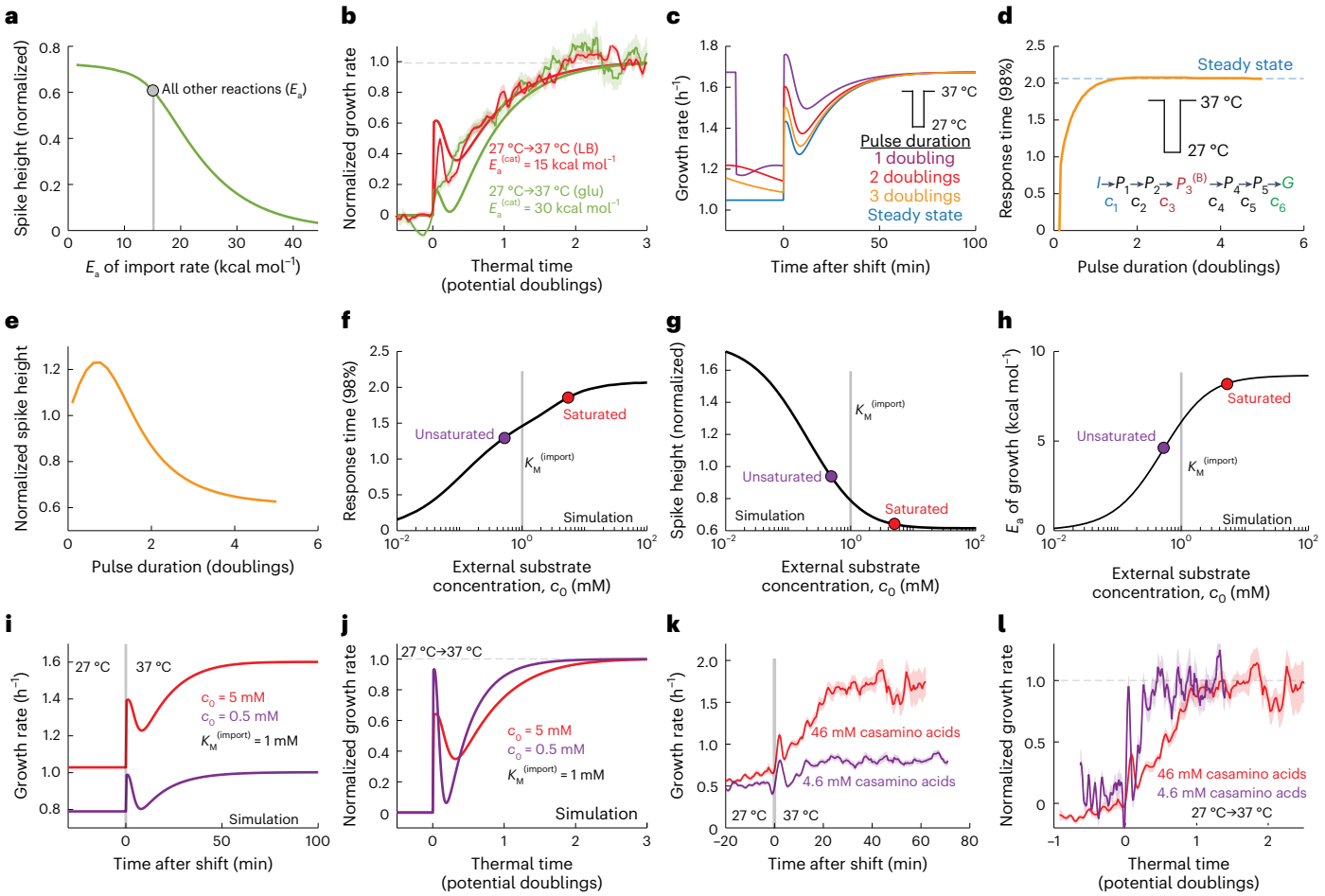

Fig. 5 | The TSEN model predicts changes to upshift response during growth on simple sugars, after a downshift pulse and at low nutrient concentration. **a**, The bottlenecked TSEN model in Fig. 4c predicts that spike height after a temperature upshift will decrease with the activation energy of import. The activation energies of all other reactions were set to 15 kcal mol^{-1} (grey circle). **b**, Increasing the activation energy of import to E_a = 30 kcal mol^{-1} on the basis of our experimental measurements of the activation energy of growth in glucose (Extended Data Fig. 9f) dramatically reduced the spike height (green) compared with our default E_a = 15 kcal mol^{-1} (red) without affecting the response time, similar to our experimental measurements of the normalized growth-rate response on glucose (green data, same as in Fig. 1h). **c**, The bottlenecked TSEN model predicts that short downshift pulses from 37 °C to 27 °C (purple, red, orange) will cause larger spikes and faster recovery to the steady-state growth rate at 37 °C than an upshift from steady state at 27 °C to 37 °C (blue), similar to our experimental observations (Fig. 1i). **d**,**e**, The bottlenecked TSEN model in Fig. 4c predicts that the response time decreases for downshift pulses of duration of <1 doubling at the higher temperature (**d**) and that the spike height remains high for pulses of duration of multiple doublings at the higher temperature (**e**). **f**–**h**, The bottlenecked TSEN model in Fig. 4c predicts that response time decreases (**f**), spike height increases (**g**) and growth activation energy decreases (**h**) when nutrient concentration is reduced from above (saturated, red circle) to below (unsaturated, purple circle) the K_M for import (grey vertical bar). **i**, Simulations of the bottlenecked TSEN model in Fig. 4c throughout an upshift from 27 °C to 37 °C for high (c_0 = 5 mM, red) or low (c_0 = 0.5 mM, purple) external substrate concentration ($K_M^{(import)}$ = 1 mM). The absolute spike height is similar in magnitude at both concentrations, but the steady-state growth rate at 37 °C is much lower for lower external substrate concentration (purple) and is reached more quickly after the upshift than for higher concentration (red). **j**, The normalized growth rate calculated from simulations in **h** has a larger spike and a faster normalized response (<1 doubling) for low external substrate concentration (purple) compared with the TSEN model at saturation (red). **k**,**l**, Growth rate throughout an upshift from 27 °C to 37 °C of *E. coli* MG1655 grown on MOPS + 46 mM casamino acids (red, n = 116 cells) or 4.6 mM casamino acids (purple, n = 261 cells) exhibits similar dynamics in both absolute (**k**) and normalized (**l**) terms as the simulations in **i** and **j**. Curves and shaded regions represent growth rate mean ± 1 s.e.m. The response time at low casamino acid concentration is much shorter (purple, ~0.25 doublings) compared with that at saturation (red, ~1.4 doublings) and is accompanied by a larger relative spike height.

response time across initial and final temperatures (Fig. 4f) as represented by linear scaling of absolute response time with doubling time at the higher temperature (Fig. 4g). This scaling was consistent with our experimental measurements (Fig. 2e), which exhibited a slope of 1.4 ± 0.3 (Fig. 4h) and the range of normalized response times measured across temperatures and growth media (Fig. 1f,h), with potential saturation at longer doubling times (>45 min).

Recent studies have shown that the metabolome is highly dynamic under nutrient perturbations[53,54], similar to the effect of temperature perturbations predicted by our TSEN model (Fig. 4e). An extension of our bottlenecked TSEN model (Fig. 4c,e) predicts that a large nutrient pulse from a low-nutrient condition should induce an increase in both growth rate and intracellular metabolite concentrations, coincident with semi-linear consumption of the external nutrient (Extended Data Fig. 8b), in qualitative agreement with glucose pulse experiments involving *E. coli*[53]. Simulations of the bottlenecked TSEN model shifted from a starvation state (c_0 = 0.01 mM) to excess nutrients (c_0 = 100 mM) induced a smooth increase in metabolite concentrations over 30–60 min (Extended Data Fig. 8c), quantitatively similar to metabolite dynamics during starvation exit in *E. coli*[54]. These results

indicate that the TSEN model is capable of recapitulating metabolomic trajectories under nutrient perturbation.

The TSEN model predicts spike dependence on nutrient type

Bacterial growth rate depends on nutrient concentration c in a manner remarkably similar to Michaelis–Menten enzyme kinetics[55], with growth rate g saturating at g_{max} when $c \gg K_M$:

$$g = \frac{g_{max} c}{K_M + c}. \quad (4)$$

This relationship (known as the Monod equation) is highly similar to the steady-state growth prediction from the TSEN model (equation (3)), which predicts that g_{max} and the Michaelis constant K_M are largely determined by import. We measured g_{max} and K_M at various temperatures across a variety of media (Extended Data Fig. 9a–c and Methods), and found that the activation energy for g_{max} was substantially larger for growth on simple sugars (12–25 kcal mol^{-1}) compared with amino acids (3–15 kcal mol^{-1}, Extended Data Fig. 9c–g).

While the normalized response time for an upshift was highly similar across nutrients (Fig. 1h), as predicted by our TSEN model, the spike was much smaller or non-existent in glucose (Fig. 1h). We probed the behaviour of our TSEN model when changing the activation energy of the catalytic rate of the import reaction. Our model predicts that spike height should decrease sharply when the activation energy of import is >15 kcal mol^{-1} (Fig. 5a), while the response time increases by only ~0.1 doubling (Fig. 5b). Thus, the model predicts that activation energy differences between nutrient types (Extended Data Fig. 9f,g) are sufficient to explain differences in the initial spike behaviour observed across growth media (Fig. 1g,h).

The TSEN model predicts metabolically encoded temperature memory

While growth rate rapidly decreases after a downshift in our model (Fig. 4d), the concentration of metabolites requires dilution to equilibrate, which takes place on the timescale of growth (Supplementary Text, production-less TSEN). Thus, during a transient downshift pulse, the cell gradually transitions from the high temperature to the low temperature metabolic state, despite rapid growth deceleration. Indeed, simulations of the bottlenecked TSEN model (Fig. 4c) during a downshift pulse from 37 °C to 27 °C back to 37 °C, with variable duration at 27 °C, resulted in faster upshift responses than from the steady state at 27 °C (Fig. 5c). More than a doubling at 27 °C was required for recovery of the upshift response time (Fig. 5d) and the spike height remained higher than for an upshift from steady state for pulses of multiple doublings (Fig. 5e), again collectively consistent with our experimental data (Fig. 1i and Extended Data Fig. 4). These findings highlight the ability of our model to reproduce nearly all observed temperature-shift responses with reasonable quantitative agreement, underscoring the importance of the temperature sensitivity of import and metabolome rearrangement in upshift responses.

The TSEN model predicts upshift response at low substrate concentration

As nutrient concentrations are low in many environments, we next simulated our model in a low-nutrient regime with external concentrations below the K_M for import (that is, $c_0 < K_0$) for a temperature upshift from 27 °C to 37 °C. At $c_0 < K_0$, the relative spike height increased substantially, and the normalized response time decreased with decreasing concentration (Fig. 5f–j). This decrease in response time occurred because the increase in import rate after a temperature upshift is smaller when $c_0 \leq K_0$ compared with $c_0 \geq K_0$ (ref. 6), despite an identical increase in catalytic rates (k_i) that consume the imported metabolite. The activation energy for growth was also predicted to decrease with decreasing nutrient concentration (Fig. 5h), in agreement with our experimental measurements of growth on amino acids (Extended Data Fig. 9g).

To test these low-nutrient predictions, we shifted *E. coli* MG1655 cells from 27 °C to 37 °C during growth on different concentrations of casamino acids (CAA; Methods). With 4.6 mM CAA, a concentration near the K_M (Extended Data Fig. 9c), growth rate increased from the steady-state value at 27 °C (~0.5 h^{-1}) to that at 37 °C (~0.8 h^{-1}) after only 25 min, corresponding to 0.25 doubling times at 37 °C (Fig. 5k,l). Moreover, the spike peaked at a growth rate close to that of the 37 °C steady state (Fig. 5k). These dynamics were in reasonable agreement with the predictions of our model (Fig. 5i,j), indicating that the response to temperature shift can be modulated by nutrient concentration, owing to the properties of the import K_M.

The TSEN model captures distinct temperature shift responses in fission yeast compared with multiple bacteria

Diverse bacterial species, including *E. coli* from host organisms with distinct temperature-dependent evolutionary histories (turtle, seagull, human) and the soil-dwelling Gram-positive *Bacillus subtilis*, exhibited similar responses to upshifts as *E. coli* MG1655 (Fig. 6a,b and Extended Data Fig. 10), suggesting a general behaviour across the bacterial kingdom.

We then determined whether single-celled eukaryotes similarly responded to temperature shifts. The fission yeast *Schizosaccharomyces pombe* grows optimally at 32 °C and possesses an Arrhenius range between 22 °C and 32 °C, with E_a ~ 8 kcal mol^{-1} in rich media[56]. During a 22 °C to 32 °C upshift on the rich medium YE5S, cells exhibited a large growth-rate spike from 0.17 h^{-1} to 0.44 h^{-1}, overshooting the steady-state 32 °C growth rate(Fig. 6c). This was followed by deceleration to 0.02 h^{-1}, then rapid acceleration to the 32 °C steady-state growth rate (~0.4 h^{-1}) (Fig. 6c). The entire response dynamics lasted ~100 min, corresponding to a normalized response time of ~1.1 doublings (Fig. 6d). Thus, despite transiently decelerating to near growth halting, *S. pombe* cells were able to reach the steady-state growth rate at the higher temperature more quickly than any bacteria tested at saturating nutrient concentration.

We then tested whether these behavioural differences were consistent with our TSEN model. By systematically varying parameters, we found that enzyme networks exhibited a faster normalized response time when the E_a of the bottleneck K_M was increased to >30 kcal mol^{-1} and the bottleneck enzymatic rate was greater than those of import and growth. Moreover, a TSEN composed of 5 bottlenecked intermediate reactions resulted in a more pronounced spike and deceleration (Fig. 6d), similar to our experimental measurements (Fig. 6c,d). The large spike and deceleration were due to rapid consumption of the network's final metabolite (c_6), which could only be replenished by upstream bottlenecked metabolites (Fig. 6e). The overall faster response time was captured by the model and was due to the decrease in steady-state concentration of c_6 at higher temperature caused by the large E_a of K_M (Fig. 6e), leading c_6 (which is limiting for growth) to stabilize more quickly.

With the same set of parameters, this TSEN model also predicted an undershooting to below the new steady-state growth rate upon a temperature decrease from 32 °C to 22 °C (Fig. 6f), a non-intuitive behaviour we confirmed experimentally (Fig. 6f). These findings suggest that the qualitatively distinct characteristics of the *S. pombe* temperature shift responses can be captured in a TSEN model by increasing the magnitude of K_M parameters and the number of bottleneck reactions. More generally, they show that the growth network can be tuned to alter the balance between certain trade-offs to accelerate responses at the cost of temporary growth stalling.

Discussion

Here we used high-precision temperature control and single-cell analyses to show that bacteria exhibit a characteristic growth-rate

https://doi.org/10.1038/s41564-024-01841-4

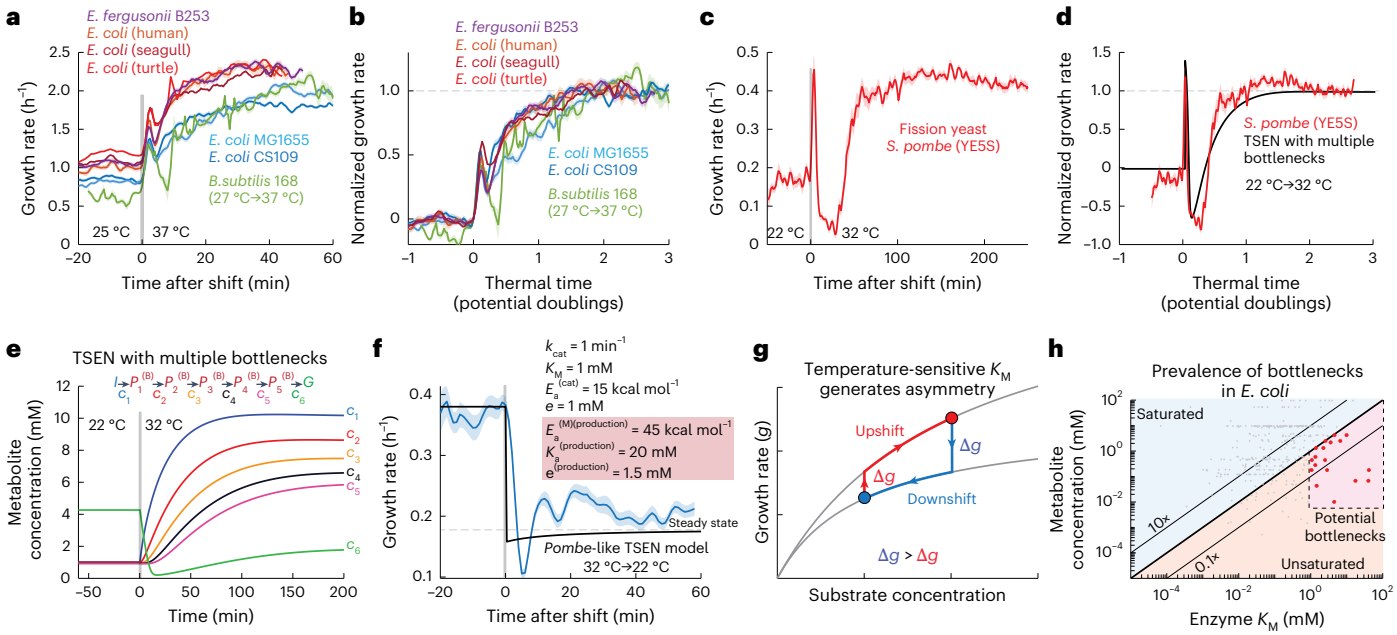

Fig. 6 | Temperature upshift response features are generally conserved across microbes and can be captured by the TSEN model. a, Growth-rate response to a temperature upshift on LB of laboratory-evolved *E. coli* (light and dark blue, $n = 773–1,279$ cells) and natural isolates from various hosts (orange to red, $n = 389–547$ cells), *Escherichia fergusonii* (purple, $n = 997$ cells) and *Bacillus subtilis* (green, $n = 236$ cells). All upshifts were from 25 °C to 37 °C, except for *B. subtilis* (27 °C to 37 °C). Curves and shaded regions represent growth rate mean ± 1 s.e.m. **b**, Normalized growth rate followed a similar trajectory versus thermal time across all strains/species for the data in **a**. **c**, A temperature upshift from 22 °C to 32 °C on the rich growth medium YE5S caused the growth rate of the fission yeast *Schizosaccharomyces pombe* to initially spike close to the steady-state value at 32 °C, then decelerate to below the steady-state value at 22 °C, then accelerate back to the new steady-state value within less than a doubling (~100 min) (red, $n = 333$ cells). Curves and shaded regions represent growth rate mean ± 1 s.e.m. **d**, A TSEN model with 5 intermediate reactions, each with a large (20 mM) and highly temperature-sensitive K_M ($E_a^{(M)} = 22.5$ kcal mol^{-1}), produces similar normalized growth rate dynamics with thermal time (black) as the *S. pombe* data in **c** (red), characterized by a large spike, deceleration to <0 and fast recovery within <1 doubling. **e**, The TSEN model in **d**, composed entirely of bottlenecks, predicts that a temperature upshift results in a rapid, large decrease in the final intermediate metabolite concentration (c_6), followed by a slower increase to the new steady-state, which is lower than that at lower temperature. All other metabolite concentrations ($c_{1–5}$) increase monotonically towards their steady-state levels at rates that depend inversely on their network depth (that is, c_5 increases more slowly than c_1). **f**, An extended TSEN model with five intermediate reactions, each with a large (20 mM) and highly temperature-sensitive ($E_a = 22.5$ kcal mol^{-1}) K_M, predicts a temporary undershoot (black) upon a downshift to growth rates below the steady-state value at the lower temperature. The fission yeast *Schizosaccharomyces pombe* exhibited an undershoot during a downshift from 32 °C to 22 °C on rich medium (YE5S) (blue, $n = 54$ cells) similar to model predictions. Experimental data are the mean ± 1 s.e.m. (shaded region) at each time point. **g**, Asymmetry in growth-rate response to temperature up- and downshifts is caused by the temperature sensitivity of K_M. If substrate concentration is near the K_M and $E_a^{(M)} > 0$, an upshift causes a small initial increase in growth rate, followed by a slow increase in substrate concentration to the new K_M via production (red). Conversely, a downshift causes a comparatively larger initial decrease in growth rate, followed by a slow decrease in substrate concentration to the new K_M via dilution (blue). **h**, Intracellular metabolite concentrations are generally much higher than the K_M of their production enzyme for *E. coli* grown on glucose (data from ref. 68). However, some metabolites have concentrations near or below the K_M of their production, and potential bottlenecks (dashed region, red points) are those with $K_M > 1$ mM and substrate concentration $c < K_M$.

response to temperature shifts within the Arrhenius range (Figs. 1c and 6a), with adaptation to an upshift requiring ~1.5 doublings at the final steady-state growth rate. The maintenance of the proteome across temperatures (Fig. 2) and the conservation of response dynamics during upshifts across mutants (Fig. 2g and Supplementary Fig. 6i) and antibiotic treatments (Fig. 3h and Extended Data Fig. 3f,g) collectively argue against the existence of a single regulator of growth rate across Arrhenius temperatures. Nonetheless, specific factors, including ppGpp production (Supplementary Fig. 7f,g), regulation of protein folding by DnaK (Extended Data Fig. 3d,e), fatty acid synthesis (Fig. 3h) and putative ribosome-dependent action by Uup (Fig. 3f), are necessary for fast and efficient upshift responses, probably indicating regulatory contributions that will need to be elucidated in future studies. Revealing these potential regulatory factors required detailed single-cell analysis, as their effects on temperature-shift responses were too subtle to emerge in genetic screens or required the deletion of multiple genes (ppGpp).

Ultimately, the ability of our TSEN model to recapitulate nearly all observed behaviours (Figs. 4 and 5, and Extended Data Fig. 7) indicates that temperature sensitivity of growth is largely a collective property of the metabolic network, which encodes a memory of temperature states (Figs. 1i and 5c, and Extended Data Fig. 4). Furthermore, a simplified version of the model predicts that the timescale of response to temperature upshifts should be ~1.4 doublings at the final steady-state growth rate (Supplementary Text and Extended Data Fig. 7c–f), regardless of details about the kinetics of import and growth. At steady state, the TSEN model predicts that growth depends only on substrate import kinetics and the total intracellular metabolite pool (equation (3)), providing a simple framework that connects concentration-dependent growth directly to measured transporter kinetics[57]. Thus, our work establishes a mechanism for how Arrhenius-like growth arises across organisms[4] (Fig. 1a, Extended Data Figs. 1 and 7g, and Supplementary Fig. 1).

A key feature of the TSEN model is the temperature dependence of K_M, which provides a straightforward mechanism for the asymmetry between upshift and downshift responses (Fig. 6g): if the substrate concentration of a reaction is near the K_M at 27 °C (Fig. 6g, blue circle), an upshift to 37 °C will be accompanied by a small instantaneous

growth rate increase since K_M is higher at 37 °C versus 27 °C; vice versa, a downshift from the K_M at 37 °C (Fig. 6g, red circle) will result in a larger instantaneous change in growth rate (Fig. 6g). Each of these instantaneous changes is then followed by an increase (upshift) or decrease (downshift) in the substrate concentration, and thus the growth rate (Fig. 6g), as predicted by the TSEN model (Fig. 4e and Supplementary Text). The temperature upshift response is predicted to be largely insensitive to the K_M of import at substrate saturation (Fig. 5f), suggesting that temperature-shift responses are independent of the details of import kinetics. A temperature-sensitive K_M predicts that the E_a of growth rate decreases with substrate concentration[6] (Fig. 5h), consistent with our measurements of growth on amino acids (Extended Data Fig. 9g). Such a decrease in temperature sensitivity at low substrate concentration is predicted by the TSEN model to decrease the response time and increase the relative spike height (Fig. 5f,g,i,j), consistent with our experimental observations that decreases in amino acid concentrations resulted in faster responses to temperature upshifts and larger relative spikes (Fig. 5k,l). Thus, microorganisms confronting nutrient-poor environments may exhibit less temperature sensitivity of growth, somewhat paradoxically owing to the temperature sensitivity of K_M values.

To produce the observed initial spike in growth rate, a bottleneck reaction with a large and highly temperature-sensitive K_M was required (Fig. 4c). Previous measurements of intracellular metabolite dynamics in *E. coli* grown on glucose showed that reactions in central carbon metabolism are largely unsaturated and many reactions can exhibit large K_M values (>1 mM)[52] (Fig. 6h), indicating that the existence of such bottlenecks is highly likely. There are many potential bottleneck enzymes (Fig. 6h); those with the largest substrate concentrations are involved in aspartate consumption for amino acid (*aspC*) and pyrimidine (*pyrB*) biosynthesis, while those with the largest K_M are involved in threonine (*ilvA*) and serine (*sdaA*, *ydfG*) degradation. As several of these reactions are essential, elucidating which reactions are true bottlenecks will probably require a combination of CRISPRi manipulation of gene expression, direct measurements of intracellular metabolite concentrations[52] and biochemical characterization across temperatures.

In addition, the TSEN model was able to explain qualitatively distinct temperature shift responses in the fission yeast *S. pombe*, which responded to an upshift with overshooting and deceleration (Fig. 6c), but which ultimately reached its steady-state growth rate faster than bacteria (Fig. 6d). The TSEN model predicted that large coupled bottleneck reactions account for this behaviour (Fig. 6d,e), and such a model predicted the undershoot response to a temperature downshift (Fig. 6f). In this scenario, faster temperature-shift responses come at the cost of increasing the activation energy of growth (Fig. 6c,f), suggesting trade-offs between fast steady-state growth across temperatures and the ability to respond quickly to shifts between temperatures.

Taken together, these findings suggest that metabolite flux rather than proteome rearrangement underlies growth rate adaptation across Arrhenius temperatures. As a result, cells adapt to temperature fluctuations without additional protein synthesis, resulting in transient memory of previously experienced temperatures (Figs. 1i and 5c–e, and Extended Data Figs. 4 and 5). Increasing protein concentrations is metabolically expensive and simulations of our TSEN model explicitly including protein synthesis confirmed that enzyme concentrations remain virtually constant throughout temperature shifts (Supplementary Fig. 8), similar to previous models of responses to nutrient perturbations[58]. The conservation of growth rate responses across organisms (Fig. 6a–d) and the ability of the TSEN model to capture diverse responses to temperature shifts (Figs. 4–6) suggest an evolutionary pressure to adopt this strategy. The ability of *E. coli* cells to withstand fluctuations across a large range of temperatures, even short pulses at heat- and cold-shock temperatures (Extended Data Fig. 5b,c,e), indicates a robustness that may be particularly important in the context of host colonization and infection-induced fevers, and our findings indicate that investigations of temperature adaptation can provide key insight into the metabolic factors limiting growth.

Methods

Culturing conditions and bacterial strains

E. coli wild-type and isolate strains were grown directly from 25% glycerol stocks stored at −80 °C in target media without selection. In typical temperature upshift experiments, cells were grown initially at 37 °C from frozen stocks overnight until saturation, then diluted 1:200 into fresh media at 37 °C until log phase (1.5–2 h in LB, ~4 h in MOPS + glucose). Cells were then diluted 1:10 into fresh media and grown for at least 3 doublings at the lower, target temperature before performing a temperature upshift.

Most mutants (for example, Keio collection knockouts) were grown from frozen stocks in target media with antibiotic selection. The ppGpp null strain (*spoT::cat, relA::kan*) was grown on LB plates with 10 μg ml^{-1} chloramphenicol and 25 μg ml^{-1} kanamycin overnight at 37 °C, and individual colonies were selected for further liquid culturing under selection to avoid suppressor mutations.

To evaluate growth kinetics on various media, *E. coli* MG1655 was first grown with shaking overnight at 37 °C in MOPS minimal medium (Teknova) adjusted to pH 7.2 and supplemented with 0.2% (w/v) D-glucose. To measure growth at lower temperatures (25 °C, 30 °C), cells were then diluted 1:200 in fresh MOPS + glucose and grown with shaking until saturation for an initial passage at the target temperature. One millilitre of cells was washed in MOPS buffer (pH 7.2) at room temperature and 1 μl was added to 200 μl of target medium in 96-well plates for generating growth curves at the target temperature in a plate reader.

All strains used in this study are listed in Supplementary Table 1.

Liquid growth curves and analysis

Growth curves were measured using a protocol developed for accurately determining growth rates at low optical density[28]. Briefly, 200 μl of medium (without bacteria) were placed into each well of a transparent 96-well plate (Greiner Bio-One) and sealed with a transparent film (Excel Scientific) with holes for gas exchange cut above each well using a laser cutter (Epilog). Optical density (OD) was measured with a BioTek Epoch 2 microplate spectrophotometer (Agilent) for at least 15 min to obtain blank values for each well at the target temperature. The seal was then removed, bacterial samples were added into each well and the plate was sealed with a fresh laser-cut transparent film. Linear and orbital shaking were conducted between OD readings, which were taken every ~7 min. The OD was corrected for nonlinearity (linear range = 0–0.6) via a serial dilution of concentrated cells and performing a polynomial fit to obtain general fit parameters[28]. For each well, the well-specific blank OD value determined before addition of cells was subtracted from the OD at each time point, which was then used to compute growth rate as a moving linear regression of the logarithm of the blanked OD.

E. coli natural isolates

E. coli strains from non-human hosts were previously isolated[24,25,59] from faecal samples (collected from a variety of sources, including park and pet store animals and domestic pets), which were grown on Colilert-18 medium (IDEXXE) for selection of presumptive *E. coli* colonies[25]. Isolate identities were confirmed by beta-glucuronidase activity and subsequent sequencing of the corresponding gene, *uidA*[25]. The strains were grown overnight in a rich medium (LB) at 37 °C, diluted 1:200 in fresh LB and grown for 24 h across temperatures from 27 °C–47 °C to measure activation energies.

Temperature-controlled single-cell imaging

The temperature control platform, named single-cell temperature controller (SiCTeC), was designed and described previously[29]. Briefly, a ring-shaped Peltier module (TE Technology) was adhered to a glass slide,

and the sample temperature was monitored on the coverslip and controlled using a micro-Arduino with a proportional-integral-derivative (PID) algorithm. Sample temperature was monitored and visualized in real time using the open-source software 'Processing'[60]. Agarose hydrogels were prepared by boiling 3% ultrapure agarose (Sigma Aldrich) in the target medium, and 200 µl of the mixture were pipetted onto a 9-mm-diameter silicone gasket (Grace Bio-Labs) onto the temperature-controlled glass slide. An additional slide was placed on the gasket to compress the hydrogel, which then cooled and solidified at the initial temperature of the experiment. After removing the additional compressing slide, 1 µl of cells was pipetted onto the solidified hydrogel and dried briefly (<1 min) at the initial temperature of the experiment.

Imaging was performed on a Ti-Eclipse microscope in phase-contrast mode using a ×40 Ph2 air objective (NA 0.95) (Nikon) with a ×1.5 tube lens. The air objective was used to avoid heatsink issues with oil-immersion objectives. Images were captured every 30 s on a Zyla 4.2 sCMOS (Andor Technology), Neo 5.5 sCMOS (Andor Technology) or PCO Panda 4.2 (Excelitas) scientific camera. The microscope system was integrated using µManager v.1.41 (ref. 61).

Image analysis

To extract cell morphology information throughout the experiment, subpixel-resolution cellular contours were obtained through a combination of deep learning-based and traditional image segmentation software[29,62]. Briefly, we first aligned the images using the template-matching plugin in FIJI[63,64], then each image was processed with a fully convolutional neural network model, 'DeepCell'[62]. Separate neural networks were trained for *E. coli* rich medium, *E. coli* minimal medium and *S. pombe* rich medium, with >200 cells manually annotated in each condition[29,62,65]. Outputs from the DeepCell classification were used to extract cellular contours using Morphometrics v.1.1 in MATLAB (MathWorks)[66]. Custom MATLAB scripts were used to track individual cells and measure cellular geometry[65].

Single-cell growth rate measurements

Cellular trajectories were filtered on the basis of the number of frames and the quality. Each trajectory was required to be ≥10 frames, over which cell length was smoothed twice with a window of four frames for rich media and 10 frames for minimal media. Instantaneous growth rate was computed by performing a windowed linear fit to the logarithm of cell length over four frames for rich media or 10 frames for minimal media, a procedure that resulted in ~1% error when recalculating expected cell lengths (Supplementary Fig. 2). Trajectories were then removed if they contained growth-rate outliers (>3 h^{-1} or <−0.1 h^{-1}), as such outliers probably indicated tracking errors. The filtered trajectories were binned at each time point to evaluate single-cell growth-rate behaviours at the population level, and the error at each time point was defined as the standard error of the mean.

Rapid temperature downshifts

To increase the rate of temperature change during downshifts from previous experiments performed using ambient temperature as the cooling sink, which required ~5 min from 37 °C to 27 °C (ref. 29), we used dry ice (solid CO_2) to rapidly cool samples. During a downshift, the SiCTeC device was powered off and a 250-ml beaker with dry ice was used to pour sublimating dry ice directly onto the sample on the glass slide. For downshifts to temperatures above ambient, when the temperature was ~1 °C above the target downshift temperature, the SiCTeC device was powered back on and the PID algorithm restarted control of the sample temperature. The sample temperature was closely monitored and adjusted accordingly for undershooting. This method enabled stabilization at the lower temperature within <1 min. For downshifts to temperatures below ambient, dry ice was continuously poured onto the sample at intervals necessary to maintain the target temperature. Temperature upshifts back to 37 °C were performed by turning the SiCTeC device back on.

Anaerobic growth

To perform temperature shifts in anerobic conditions, *E. coli* MG1655 was inoculated from a frozen stock into LB and grown overnight in an anaerobic chamber (Coy Laboratory), then diluted 1:200 and grown until saturation in pre-reduced LB (that is, kept in the chamber for >48 h before culturing). Cells were diluted 1:200 in pre-reduced LB and grown at 37 °C until log phase (~2 h), then diluted 1:10 and grown at 27 °C for 3 h. From log phase at 27 °C, 1 µl was pipetted on a SiCTeC glass slide for temperature shifts (all components pre-reduced) and imaged inside the chamber using a Ti-Eclipse inverted microscope (Nikon) with a Neo 5.5 sCMOS (Andor Technology). The SiCTeC platform was controlled by a laptop inside the chamber.

Quantification of response time

The steady-state growth rate (g_{ss}) at the final temperature was determined by measuring the average of the growth rates across the time points after which growth rate had stabilized (determined by visual inspection). The growth rate was then normalized according to $\frac{g(t)-g(0)}{g_{ss}-g(0)}$, where $g(0)$ is the growth rate immediately before the temperature shift (Fig. 1e). The time was also converted to a 'thermal time' (Fig. 1e), wherein the time was divided by the doubling time at the final steady-state growth rate ($\tau_D = \frac{\ln(2)}{g_{ss}}$). A weighted linear fit was then performed over the linear portion of the upshift response (25–95% of g_{ss}), and the response time (τ_R) was defined as the point at which the linear fit equalled one ($g(\tau_R) = g_{ss}$). The error in the response time was generated from the 95% confidence interval of the fitted slope.

Antibiotic treatment during single-cell temperature shifts

Aliquots (500 µl) of growth medium + 3% ultrapure agarose were melted at 95 °C, then mixed with 0.5 µl of 1,000× target concentration antibiotic stock solution, and 150 µl was immediately used to make a hydrogel for the sample as described above. The short time exposure to higher temperatures (~30 s) probably only moderately impacted the minimum inhibitory concentration, as antibiotic efficacies against *E. coli* are unaffected by long-term (30 min) treatment at 56 °C, with many drugs unaffected by autoclaving (121 °C)[67].

Liquid-culture samples for proteome extraction

E. coli MG1655 was grown at 37 °C overnight in MOPS buffer (Teknova) adjusted to pH 7.2 and supplemented with 0.2% (w/v) of carbon source (glucose or glycerol) (Sigma Aldrich) or LB (Thermo Fisher), then diluted in duplicate and grown for at least 4 doublings at the target temperature (25 °C, 30 °C or 37 °C). Growth at additional temperatures (16 °C, 43 °C) was assayed for LB. Cultures were grown to log phase ($OD_{600} \approx 0.2$) in 50-ml Falcon tubes, and 15 ml were collected and washed with 1 ml PBS via centrifugation at 4 °C. Supernatant was removed and the pellet was snap frozen with liquid nitrogen.

Proteome extraction

Extraction was performed as previously described[68]. Briefly, samples were thawed and lysed using a bead-beating procedure, then supernatant was reduced and alkylated with dithiothreitol and iodoacetamide, respectively. Peptides were then washed, digested and eluted using S-trap tubes (Protifi) and desalted with C18 solid-phase extraction (Sep-Pak Waters). Finally, peptides were dried by vacuum centrifugation and quantified for normalization (Nanodrop ND-1000).

Proteomic analysis via LC–MS/MS and database searching

Peptide quantification was performed following previous work[68]. Dried peptides were diluted in 0.2% formic acid to a final concentration of 0.5 µg ml^{-1}, and 1 µl was loaded onto an in-house laser-pulled

100-µm (inner diameter) nanospray column packed to ~22 cm with ReproSil-Pur C18-AQ 3.0-µm resin (Dr. Maisch). Peptides were separated by reversed-phase chromatography (Dionex Ultimate 3000 HPLC, Thermo Fisher); buffer A of the mobile phase contained 0.1% formic acid in HPLC-grade water and buffer B contained 0.1% formic acid in acetonitrile. HPLC used a two-step linear gradient with 4–25% buffer B for 135 min, followed by 25–45% buffer B for 15 min at 0.300 µl min^{-1}. Peptides were then directed to an LTQ Orbitrap Elite mass spectrometer (Thermo Fisher) in data-dependent mode, with full MS scans acquired in the mass analyser with a resolution of 60,000 and m/z range of 340–1,600. The top 20 most abundant ions with intensity thresholds >500 counts and charge state >2 were selected for fragmentation using collision-induced dissociation (CID) with an isolation window of 2 m/z, normalized collision energy of 35%, activation Q of 0.25 and activation time of 5 ms. CID fragments were analysed in the ion trap with rapid scan rate, and dynamic exclusion was enabled with a repeat count of 1 and exclusion duration of 20 s. The AGC target was set to 1,000,000 and 50,000 for full FTMS and ITMSn scans, respectively, and the maximum injection time was set to 250 ms and 100 ms for full FTMS and ITMSn scans, respectively.

Mass spectra were searched against the UniProt canonical *E. coli* FASTA database using the SEQUEST algorithm of Proteome Discoverer 2.2.0.388. The search was performed against the UniProt canonical *E. coli* FASTA database, along with a database containing common preparatory contaminants. The precursor mass range was set to 350–3,000 Da, mass error tolerance to 10 ppm and fragment mass error tolerance to 0.6 Da. Enzyme specificity was set to trypsin, and carbamidomethylation of cysteines (57.021) was set as a variable modification. Oxidation of methionines (+15.995) and protein N-terminal acetylation (+42.011) were considered as variable modifications. Peptides were filtered using Percolator, with the protein false discovery rate set to 1%. Protein abundance was based on precursor ion peak areas.

Proteome data analysis and annotation using Clusters of Orthologous Groups (COG)

Protein functional annotation was performed using the COG database[69]. UniProt accession codes were mapped to the COG database downloaded from https://ftp.ncbi.nih.gov/pub/COG/COG2014/data/. After removing non-bacterial groups, COGs were reduced to 9 functional groups: ribosomal protein (RP), non-RP translational, transcription, DNA replication, cell division, cell envelope structure, post-translational modification, energy and metabolism, and other. The corresponding gene of each protein was annotated using the gene association table from EcoCyc (https://ecoliwiki.org/gaf/gene_association.ecocyc.gz)[70].

Relative protein abundance (that is, proteome fraction) within each sample was calculated by normalizing across all protein abundances from the sample, and the mean relative protein abundance was then calculated across biological replicates. Proteins were excluded if they were only detected in one of the biological replicates. The significance threshold for changes in mean relative abundance of a single protein was defined as 2-fold, and hits were excluded if the relative difference between replicates was greater than the mean relative difference between replicates across all proteins (14–20% across samples).

E. coli transposon library temperature shifts

One millilitre of a pooled library of *E. coli* BW25113 transposon insertion mutants with random DNA barcodes[41] was thawed, diluted into 50 ml of LB + 25 µg ml^{-1} kanamycin (Sigma Aldrich) in a 250-ml Erlenmeyer flask (Pyrex) and grown with shaking overnight at 37 °C. A volume of 0.5 ml of the stationary-phase library cultures was diluted into 50 ml of LB in technical replicates at 25 °C and 37 °C.

The 25 °C culture was grown for 3 h to early log phase (OD_{600} ≈ 0.15) and 6 ml were diluted into each of two flasks containing 50 ml fresh LB pre-warmed at 25 °C, then grown for another 3 h in an air-heated shaker (New Brunswick Scientific). The temperature upshift from 25 °C to 37 °C was performed by placing one of the 25 °C flasks into a heated water shaker at 37 °C. The control sample was left at 25 °C. Samples were collected in 1.5-ml aliquots and flash frozen using liquid nitrogen every 10 min at timepoints of −10, 0, 10, 20, 30, 40, 60, 90 min relative to the shift (control samples without temperature shifts were also taken at the same time points).

The 37 °C culture was grown for 2 h until mid- to late-log phase (OD_{600} ≈ 0.3) and 1.5 ml were diluted into each of two flasks containing 50 ml of fresh LB pre-warmed at 37 °C, then grown for ~1 h in a heated water shaker. For the temperature downshift from 37 °C to 25 °C, one of the flasks was first placed into a room-temperature water bath for 6 min for faster cooling, then transferred to an air-heated shaker at 25 °C. The other flask was maintained at 37 °C as a control.

Each set of downshift/upshift experiments was performed twice, and all samples were flash frozen and immediately stored at −80 °C. Optical density was monitored at each time point for all experiments with a Genesys 20 spectrophotometer (Thermo Fisher). The timescale of the temperature upshift was estimated to be ~3.5 min using a virtual experiment with 50 ml of water in a flask, whose temperature was directly monitored during a shift from 25 °C to 37 °C using the SiCTeC device thermistor reading. A similar test was performed for the 37 °C to 25 °C downshift by placing a 37 °C flask with 50 ml of water into a stationary water bath at room temperature, giving an estimate of ~6 min to complete the temperature shift.

E. coli transposon mutant library sequencing and analysis

Barcode sequencing (BarSeq) was performed as previously described[41]. Briefly, genomic DNA was extracted using the DNeasy 96 Blood and Tissue kit (Qiagen) and quantified using the Quant-iT dsDNA BR Assay kit (Qiagen). BarSeq PCR was performed using 200 ng of genomic DNA template in 150-µl reaction volumes with Q5 polymerase (with enhancer) (New England Biolabs), 20 µM forward P5 primer and 20 µM reverse P7 primers (Supplementary Table 2) with 6-bp TruSeq indices that are automatically demultiplexed by Illumina software. PCR products were checked for completion using gel electrophoresis, and 10 µl of each reaction product were pooled and purified using the Zymo DNA Clean and Concentrator kit (Zymo). Sequencing was performed at the Chan Zuckerberg BioHub facility on an Illumina NextSeq 550 platform in high output mode.

BarSeq analysis was performed as previously detailed[41], with relevant scripts available at https://genomics.lbl.gov/supplemental/rbarseq/. Briefly, barcode reads were mapped to their corresponding genomic loci using sequencing of the transposon insertions in the *E. coli* library, and genes were filtered for those with ≥10 barcodes in the central (10–90%) portion of the gene. Temperature-shift samples were analysed along with their corresponding unshifted control samples, with the time-zero sample corresponding to when the library was shifted (t = 0 sample). The fitness of each mutant was measured as the $\log_2$fold-change in its relative abundance, and further analysis was performed using custom MATLAB scripts. Significance was defined as ≥2-fold difference in relative abundance during a temperature shift.

FRAP measurements

E. coli cultures were grown overnight from frozen stocks at 37 °C in LB, with 25 µg ml^{-1} kanamycin selection for Δ*fabR* and Δ*fadR* mutants, and then diluted 1:200 into fresh LB and grown until log phase at 37 °C (~2 h). Cultures were then diluted 1:10 into fresh LB, and 2 µl of 0.5 mg ml^{-1} MitoTracker Green (Thermo Fisher) were added. The culture was grown at the target temperature for 30 min to enable sufficient membrane labelling. Stained cells (500 µl) were washed via centrifugation (30 s at 7,000 g) in fresh LB at the target temperature (37 °C or 27 °C). One microlitre of washed culture was placed on an LB 3% agarose hydrogel and prepared for imaging using the standard glass slide technique. Imaging was performed with a Zeiss LSM 880 confocal microscope with an environmental chamber for monitoring and

controlling temperature (37 °C) and integrated with the ZEN software suite (Zeiss). Temperature upshift experiments were performed by placing the sample into the heated environmental chamber for 5 min before imaging. Fluorescence recovery after photobleaching (FRAP) of individual cells was performed with excitation at 488 nm using the ZEN software by choosing a photobleaching region near cell tips covering 1/4 to 1/3 of the cell. The entire cell was imaged at minimum frame intervals (150–300 ms) to image fluorescence recovery.

FRAP analysis and viscosity estimate

Individual regions of interest were manually delineated for the photobleached cell tips and the entire cell in FIJI[64], and the total fluorescence of each area was quantified at each time point. These data were imported for further analysis in MATLAB. The fluorescence recovery in each photobleached region was corrected by the rate of photobleaching in the entire cell, and the recovery curve was normalized and fit to the exponential function $(1-e^{-\frac{t}{\tau_D}})$. The time constant ($\tau_D$) was used to estimate a diffusion coefficient (D) via solution to Gaussian photobleaching in a plane, $\tau_D = \frac{r^2}{4D}$ (that is, modelling the cell tip as a disk of radius r on the membrane)[71]. Viscosity (η) was calculated using the Stokes–Einstein equation ($\eta = \frac{k_B T}{6\pi R D}$), where R is the radius of the fluorophore (estimated as 2 nm).

Schizosaccharomyces pombe culturing

S. pombe WT972 h- was grown from a frozen stock on YE5S plates (5 g l^{-1} yeast extract, 30 g l^{-1} glucose, 225 mg l^{-1} each of adenine, histidine, leucine, uracil and lysine hydrochloride, 2% Difco Bacto Agar). A single colony was grown at 22 °C or 32 °C in liquid YE5S overnight until saturation, then diluted 1:100 and grown until log phase ($OD_{600} \approx 0.3$–0.5). One microlitre of log-phase cells was placed on a 3% agarose YE5S pad at the initial temperature of the experiment for imaging.

Estimate of LB molarity

LB is largely composed of free amino acids, and measurements of *E. coli* auxotrophy and direct HPLC quantification[70] have provided an estimate of ~122 g mol^{-1} for its free amino acid content. The molar mass of tryptone is reported by the manufacturer to be 71.08 g mol^{-1} (Thermo Fisher). As LB is composed of 10 g tryptone and 5 g yeast extract dissolved in 1 l H_2O, we estimate that the concentration of metabolizable free amino acids in LB is ~182 mM. Note that the accuracy of this estimate is not critical for any of our conclusions; the value simply enables plotting of LB concentrations on the same plot as other substrates such as casamino acids.

Measurements of K_M

E. coli MG1655 was grown overnight until saturation in MOPS buffer + 0.2% (w/v) glucose at the target temperature (25 °C, 30 °C, 37 °C), then washed twice in MOPS buffer before being diluted 1:200 in the target medium at the target temperature. Liquid-culture growth curves were obtained as described above. OD was measured using a microplate reader and maximal growth rate was quantified as the peak of the derivative of ln(background-subtracted OD)[28]. A weighted fit was performed on the growth rate versus concentration curve using the Monod equation (equation (4)) to extract an estimate of K_M with a standard error. We note that it was challenging to obtain growth rates at low concentration for simple sugars (for example, glucose, fructose) due to both the low K_M and generally low growth rate (<0.2 h^{-1}) (Extended Data Fig. 9a–c). In succinate, the relationship between ln(growth rate) and $1/T$ appeared bilinear, thus a linear fit produced an estimate of E_a with very large standard error (19 ± 14 kcal mol^{-1}) (Extended Data Fig. 9f).

Evaluation of the quality of growth rate measurements

The cell length corresponding to each filtered growth-rate trajectory was predicted by integrating the computed growth rate, g, as follows:

$$\begin{aligned} g &= \frac{1}{L}\frac{\mathrm{d}L}{\mathrm{d}t} \\ \Rightarrow \int_{L(0)}^{L(t)} \frac{\mathrm{d}L}{L} &= \int_0^t g(t')\,\mathrm{d}t' = G(t) \\ \Rightarrow L_\mathrm{e}(t) &= L(0)e^{G(t)}. \end{aligned} \tag{5}$$

By computing $G(t)$ at each timepoint, t, the expected length, $L_e(t)$, can be predicted from the trajectory's initial cell length, $L(0)$. The error of the expected length over time, $E(t)$, is defined as the relative difference from the measured cell length, $L_m(t)$:

$$E(t) = \frac{|L_\mathrm{m}(t) - L_\mathrm{e}(t)|}{L_\mathrm{m}(t)}. \tag{6}$$

We found that the predicted cell lengths were extremely highly correlated with measured cell lengths throughout temperature-shift experiments ($r = 0.999$, Supplementary Fig. 2c), with <1% error that depends on the growth rate ($r = 0.58$, Supplementary Fig. 2d).

Sensitivity analysis of the functional genetic screen

To determine the difference in response time of a mutant relative to wild type sufficient to produce a 2-fold difference in relative abundance after a temperature upshift (Fig. 3), we assumed that the upshift response is approximately linear (Fig. 1f). In this case, the biomass, B, varies with growth rate, g, as

$$g = \frac{\mathrm{d}(\ln(B))}{\mathrm{d}t}. \tag{7}$$

Upon a temperature upshift, the growth rate varies from g_i to g_f over a time τ_R, and the experiment is carried out over a time $t_f > \tau_R$. Hence,

$$\begin{aligned} \int_{\ln(B_1)}^{\ln(B_2)} \mathrm{d}(\ln(B)) &= \int_0^{\tau_R} \left(g_i + \tfrac{g_f - g_i}{\tau_R}t\right)\mathrm{d}t + \int_{\tau_R}^{t_f} g_f \mathrm{d}t \\ \Rightarrow \ln\left(\tfrac{B_2}{B_1}\right) &= g_f t_f - \tfrac{1}{2}(g_f - g_i)\tau_R. \end{aligned} \tag{8}$$

Consider a mutant that has the same initial and final growth rates as wild type (that is, the mutant is present in the mutant pool at both temperatures), but possesses a different response time, τ'_R. Then its final biomass, B'_2, after an upshift will be

$$\ln\left(\frac{B'_2}{B_1}\right) = g_f t_f - \frac{1}{2}(g_f - g_i)\tau'_R. \tag{9}$$

The difference in biomass between the mutant and wild type will then be

$$\ln\left(\frac{B_2}{B'_2}\right) = \frac{1}{2}(g_f - g_i)(\tau'_R - \tau_R). \tag{10}$$

Since we defined the significance threshold for our screen as a 2-fold difference in biomass and the wild-type response time is ~1.5-fold the doubling time, τ_D, a longer response time implies that

$$\ln(2) = \frac{1}{2}(g_f - g_i)(\tau'_R - 1.5\tau_D). \tag{11}$$

By setting $\tau'_R = f\tau_R$ and using the relation $\tau_D = \frac{\ln(2)}{g_f}$,

$$\begin{aligned} \ln(2) &= \tfrac{1}{2}(g_f - g_i)(f-1)1.5\ln(2)/g_f \\ \Rightarrow f &= 1 + \frac{4}{3\left(1-\frac{g_i}{g_f}\right)}. \end{aligned} \tag{12}$$

The ratio of g_i/g_f for *E. coli* in rich medium is ~0.7/2.0 (Fig. 1a,b), hence $f \approx 3$. This set of calculations indicates that a >2-fold difference in biomass at $t_f > \tau'_R > \tau_R$ requires at least a 3-fold increase in the response time. While the Δ*dnaK* and *ppGpp*^{null} mutants exhibited some lag or increase in response time (Extended Data Fig. 3d–g), direct integration of the mean growth rate trajectories during a temperature upshift predicted biomass differences of ~1.5-fold, less than our transposon screen cut-off. Thus, our screening results are consistent with the small differences in growth-rate dynamics observed with the Δ*dnaK* mutant; the *ppGpp*^{null} mutant is a double mutant and hence is not represented by a mutant in the transposon library.

Reporting summary

Further information on research design is available in the Nature Portfolio Reporting Summary linked to this article.

Data availability

Imaging datasets used to generate growth rate analyses are available from the corresponding author upon request. Processed and analysed imaging data sets of growth trajectories and FRAP measurements, liquid growth measurements, processed transposon sequencing and processed proteomics data are all available at the Harvard Dataverse[72]. Raw transposon sequencing data have been deposited in NCBI's Sequence Read Archive (SRA) under project accession identifier PRJNA1138713. Mass spectrometry proteomics data have been deposited in the ProteomeXchange Consortium via the PRIDE[73] partner repository with data set identifier PXD048941.

Code availability

Codes for generating single-cell trajectories[74] and for analysing single-cell growth rates[75] are available in GitHub. Simulation code for the TSEN model is available in GitHub[76].

References

1. Zhang, Y. & Gross, C. A. Cold shock response in bacteria. *Annu. Rev. Genet.* **55**, 377–400 (2021).
2. Richter, K., Haslbeck, M. & Buchner, J. The heat shock response: life on the verge of death. *Mol. Cell* **40**, 253–266 (2010).
3. Barber, M. A. The rate of multiplication of *Bacillus coli* at different temperatures. *J. Infect. Dis.* **5**, 379–400 (1908).
4. Mohr, P. W. & Krawiec, S. Temperature characteristics and Arrhenius plots for nominal psychrophiles, mesophiles and thermophiles. *J. Gen. Microbiol.* **121**, 311–317 (1980).
5. Herendeen, S. L., VanBogelen, R. A. & Neidhardt, F. C. Levels of major proteins of *Escherichia coli* during growth at different temperatures. *J. Bacteriol.* **139**, 185–194 (1979).
6. Knapp, B. D. & Huang, K. C. The effects of temperature on cellular physiology. *Annu. Rev. Biophys.* **51**, 499–526 (2022).
7. Chen, K. et al. Thermosensitivity of growth is determined by chaperone-mediated proteome reallocation. *Proc. Natl Acad. Sci. USA* **114**, 11548–11553 (2017).
8. Phillips, R., Kondev, J. & Theriot, J. *Physical Biology of the Cell* (Garland Science, 2009).
9. Hinshelwood, C. N. On the chemical kinetics of autosynthetic systems. *J. Chem. Soc. (Resumed)* **1952**, 745–755 (1952).
10. Iyer-Biswas, S. et al. Scaling laws governing stochastic growth and division of single bacterial cells. *Proc. Natl Acad. Sci. USA* **111**, 15912–15917 (2014).
11. Elias, M., Wieczorek, G., Rosenne, S. & Tawfik, D. S. The universality of enzymatic rate-temperature dependency. *Trends Biochem. Sci.* **39**, 1–7 (2014).
12. Dill, K. A., Ghosh, K. & Schmit, J. D. Physical limits of cells and proteomes. *Proc. Natl Acad. Sci. USA* **108**, 17876–17882 (2011).
13. Lemaux, P. G., Herendeen, S. L., Bloch, P. L. & Neidhardt, F. C. Transient rates of synthesis of individual polypeptides in *E. coli* following temperature shifts. *Cell* **13**, 427–434 (1978).
14. Gadgil, M., Kapur, V. & Hu, W. S. Transcriptional response of *Escherichia coli* to temperature shift. *Biotechnol. Prog.* **21**, 689–699 (2005).
15. Tagkopoulos, I., Liu, Y. C. & Tavazoie, S. Predictive behavior within microbial genetic networks. *Science* **320**, 1313–1317 (2008).
16. Zhou, Y. N., Kusukawa, N., Erickson, J. W., Gross, C. A. & Yura, T. Isolation and characterization of *Escherichia coli* mutants that lack the heat shock sigma factor sigma 32. *J. Bacteriol.* **170**, 3640–3649 (1988).
17. Chohji, T., Sawada, T. & Kuno, S. Effects of temperature shift on growth rate of *Escherichia coli* BB at lower glucose concentration. *Biotechnol. Bioeng.* **25**, 2991–3003 (1983).
18. Sinensky, M. Homeoviscous adaptation—a homeostatic process that regulates the viscosity of membrane lipids in *Escherichia coli*. *Proc. Natl Acad. Sci. USA* **71**, 522–525 (1974).
19. Budin, I. et al. Viscous control of cellular respiration by membrane lipid composition. *Science* **362**, 1186–1189 (2018).
20. Scott, M., Klumpp, S., Mateescu, E. M. & Hwa, T. Emergence of robust growth laws from optimal regulation of ribosome synthesis. *Mol. Syst. Biol.* **10**, 747 (2014).
21. Bremer, H. & Dennis, P. P. Modulation of chemical composition and other parameters of the cell at different exponential growth rates. *EcoSal Plus* https://doi.org/10.1128/ecosal.5.2.3 (2008).
22. Belliveau, N. M. et al. Fundamental limits on the rate of bacterial growth and their influence on proteomic composition. *Cell Syst.* **12**, 924–944.e2 (2021).
23. Zaritsky, A. Effects of growth temperature on ribosomes and other physiological properties of *Escherichia coli*. *J. Bacteriol.* **151**, 485–486 (1982).
24. Ram, J. L., Ritchie, R. P., Fang, J., Gonzales, F. S. & Selegean, J. P. Sequence-based source tracking of *Escherichia coli* based on genetic diversity of beta-glucuronidase. *J. Environ. Qual.* **33**, 1024–1032 (2004).
25. Ram, J. L. et al. Identification of pets and raccoons as sources of bacterial contamination of urban storm sewers using a sequence-based bacterial source tracking method. *Water Res.* **41**, 3605–3614 (2007).
26. Arcus, V. L. & Mulholland, A. J. Temperature, dynamics, and enzyme-catalyzed reaction rates. *Annu. Rev. Biophys.* **49**, 163–180 (2020).
27. Nguyen, V. et al. Evolutionary drivers of thermoadaptation in enzyme catalysis. *Science* **355**, 289–294 (2017).
28. Atolia, E. et al. Environmental and physiological factors affecting high-throughput measurements of bacterial growth. *mBio* **11**, e01378-20 (2020).
29. Knapp, B. D., Zhu, L. & Huang, K. C. SiCTeC: an inexpensive, easily assembled Peltier device for rapid temperature shifting during single-cell imaging. *PLoS Biol.* **18**, e3000786 (2020).
30. Cashel, M. & Gallant, J. Two compounds implicated in the function of the RC gene of *Escherichia coli*. *Nature* **221**, 838–841 (1969).
31. Irving, S. E., Choudhury, N. R. & Corrigan, R. M. The stringent response and physiological roles of (pp)pGpp in bacteria. *Nat. Rev. Microbiol.* **19**, 256–271 (2021).
32. Mackow, E. R. & Chang, F. N. Correlation between RNA synthesis and ppGpp content in *Escherichia coli* during temperature shifts. *Mol. Gen. Genet.* **192**, 5–9 (1983).
33. Scott, M., Gunderson, C. W., Mateescu, E. M., Zhang, Z. & Hwa, T. Interdependence of cell growth and gene expression: origins and consequences. *Science* **330**, 1099–1102 (2010).
34. Maitra, A. & Dill, K. A. Bacterial growth laws reflect the evolutionary importance of energy efficiency. *Proc. Natl Acad. Sci. USA* **112**, 406–411 (2015).

35. Reuveni, S., Ehrenberg, M. & Paulsson, J. Ribosomes are optimized for autocatalytic production. *Nature* **547**, 293–297 (2017).
36. Hui, S. et al. Quantitative proteomic analysis reveals a simple strategy of global resource allocation in bacteria. *Mol. Syst. Biol.* **11**, 784 (2015).
37. Schmidt, A. et al. The quantitative and condition-dependent *Escherichia coli* proteome. *Nat. Biotechnol.* **34**, 104–110 (2016).
38. Li, G. W., Burkhardt, D., Gross, C. & Weissman, J. S. Quantifying absolute protein synthesis rates reveals principles underlying allocation of cellular resources. *Cell* **157**, 624–635 (2014).
39. Jones, P. G., VanBogelen, R. A. & Neidhardt, F. C. Induction of proteins in response to low temperature in *Escherichia coli*. *J. Bacteriol.* **169**, 2092–2095 (1987).
40. Grossberger, R. et al. Influence of RNA structural stability on the RNA chaperone activity of the *Escherichia coli* protein StpA. *Nucleic Acids Res.* **33**, 2280–2289 (2005).
41. Wetmore, K. M. et al. Rapid quantification of mutant fitness in diverse bacteria by sequencing randomly bar-coded transposons. *mBio* **6**, e00306–e00315 (2015).
42. Murina, V. et al. ABCF ATPases involved in protein synthesis, ribosome assembly and antibiotic resistance: structural and functional diversification across the Tree of Life. *J. Mol. Biol.* **431**, 3568–3590 (2019).
43. Cochrane, K. *Elucidating Ribosomes—Genetic Studies of the ATPase Uup and the Ribosomal Protein L1* (Univ. of Michigan, 2015).
44. Sulavik, M. C. et al. Antibiotic susceptibility profiles of *Escherichia coli* strains lacking multidrug efflux pump genes. *Antimicrob. Agents Chemother.* **45**, 1126–1136 (2001).
45. Wilson, D. N. Ribosome-targeting antibiotics and mechanisms of bacterial resistance. *Nat. Rev. Microbiol.* **12**, 35–48 (2014).
46. Ikeuchi, Y., Shigi, N., Kato, J., Nishimura, A. & Suzuki, T. Mechanistic insights into sulfur relay by multiple sulfur mediators involved in thiouridine biosynthesis at tRNA wobble positions. *Mol. Cell* **21**, 97–108 (2006).
47. Campbell, J. W. & Cronan, J. E. Jr. *Escherichia coli* FadR positively regulates transcription of the fabB fatty acid biosynthetic gene. *J. Bacteriol.* **183**, 5982–5990 (2001).
48. Borgaro, J. G., Chang, A., Machutta, C. A., Zhang, X. & Tonge, P. J. Substrate recognition by beta-ketoacyl-ACP synthases. *Biochemistry* **50**, 10678–10686 (2011).
49. Sorensen, T. H. et al. Temperature effects on kinetic parameters and substrate affinity of Cel7A cellobiohydrolases. *J. Biol. Chem.* **290**, 22193–22202 (2015).
50. Sizer, I. W. in *Advances in Enzymology and Related Areas of Molecular Biology* (eds Nord, F. F. & Werkman, C. H.) 35–62 (Wiley, 1943).
51. Ehmann, J. D. & Hultin, H. O. Temperature dependence of the Michaelis constant of chicken breast muscle lactate dehydrogenase. *J. Food Sci.* **38**, 1119–1121 (1973).
52. Bennett, B. D. et al. Absolute metabolite concentrations and implied enzyme active site occupancy in *Escherichia coli*. *Nat. Chem. Biol.* **5**, 593–599 (2009).
53. Taymaz-Nikerel, H. et al. Changes in substrate availability in *Escherichia coli* lead to rapid metabolite, flux and growth rate responses. *Metab. Eng.* **16**, 115–129 (2013).
54. Link, H., Fuhrer, T., Gerosa, L., Zamboni, N. & Sauer, U. Real-time metabolome profiling of the metabolic switch between starvation and growth. *Nat. Methods* **12**, 1091–1097 (2015).
55. Monod, J. The growth of bacterial cultures. *Annu. Rev. Microbiol.* **3**, 371–394 (1949).
56. Petersen, J. & Russell, P. Growth and the environment of *Schizosaccharomyces pombe*. *Cold Spring Harb. Protoc.* https://doi.org/10.1101/pdb.top079764 (2016).
57. Chang, A. et al. BRENDA, the ELIXIR core data resource in 2021: new developments and updates. *Nucleic Acids Res.* **49**, D498–D508 (2021).
58. Mairet, F., Gouze, J. L. & de Jong, H. Optimal proteome allocation and the temperature dependence of microbial growth laws. *npj Syst. Biol. Appl.* **7**, 14 (2021).
59. Walk, S. T. et al. Cryptic lineages of the genus *Escherichia*. *Appl. Environ. Microbiol.* **75**, 6534–6544 (2009).
60. Reas, C. & Fry, B. Processing: programming for the media arts. *AI Soc.* **20**, 526–538 (2006).
61. Edelstein, A., Amodaj, N., Hoover, K., Vale, R. & Stuurman, N. Computer control of microscopes using μManager. *Curr. Protoc. Mol. Biol.* https://doi.org/10.1002/0471142727.mb1420s92 (2010).
62. Van Valen, D. A. et al. Deep learning automates the quantitative analysis of individual cells in live-cell imaging experiments. *PLoS Comput. Biol.* **12**, e1005177 (2016).
63. Tseng, Q. et al. A new micropatterning method of soft substrates reveals that different tumorigenic signals can promote or reduce cell contraction levels. *Lab Chip* **11**, 2231–2240 (2011).
64. Schindelin, J. et al. Fiji: an open-source platform for biological-image analysis. *Nat. Methods* **9**, 676–682 (2012).
65. Knapp, B. D. et al. Decoupling of rates of protein synthesis from cell expansion leads to supergrowth. *Cell Syst.* **9**, 434–445.e6 (2019).
66. Ursell, T. et al. Rapid, precise quantification of bacterial cellular dimensions across a genomic-scale knockout library. *BMC Biol.* **15**, 17 (2017).
67. Traub, W. H. & Leonhard, B. Heat stability of the antimicrobial activity of sixty-two antibacterial agents. *J. Antimicrob. Chemother.* **35**, 149–154 (1995).
68. Shi, H. et al. Precise regulation of the relative rates of surface area and volume synthesis in bacterial cells growing in dynamic environments. *Nat. Commun.* **12**, 1975 (2021).
69. Galperin, M. Y., Makarova, K. S., Wolf, Y. I. & Koonin, E. V. Expanded microbial genome coverage and improved protein family annotation in the COG database. *Nucleic Acids Res.* **43**, D261–D269 (2015).
70. Karp, P. D. et al. The EcoCyc Database (2023). *EcoSal Plus* **11**, eesp00022023 (2023).
71. Axelrod, D., Koppel, D. E., Schlessinger, J., Elson, E. & Webb, W. W. Mobility measurement by analysis of fluorescence photobleaching recovery kinetics. *Biophys. J.* **16**, 1055–1069 (1976).
72. Knapp, B. D. Replication Data for: Metabolic rearrangement enables adaptation of microbial growth rates to temperature shifts. *Harvard Dataverse* https://doi.org/10.7910/DVN/SC2KXZ (2024).
73. Perez-Riverol, Y. et al. The PRIDE database and related tools and resources in 2019: improving support for quantification data. *Nucleic Acids Res.* **47**, D442–D450 (2019).
74. MATLAB functions for generating single-cell trajectories from Morphometrics contours. *GitHub* https://github.com/bknapp8/cell_tracking_bacteria (2024).
75. Temperature-shift growth rate analysis. *GitHub* https://github.com/bknapp8/temperature_shift_growthrate (2024).
76. Temperature-sensitive enzyme network (TSEN) model package. *GitHub* https://github.com/bknapp8/TSEN_models (2024).

Acknowledgements

We thank members of the Huang lab for helpful discussions. The *E. coli* BW25113 transposon mutant library was provided by the Deutschbauer lab (Lawrence Berkeley National Laboratory), with help from V. Trotter. This work was funded by a Stanford Interdisciplinary Graduate Fellowship (to B.D.K.), NIH RM1 GM135102 (to K.C.H.) and NSF Awards EF-2125383 and IOS-2032985 (to K.C.H.). K.C.H. is a Chan Zuckerberg Biohub Investigator.

Author contributions

B.D.K. and K.C.H. conceived the study and designed the experiments. B.D.K. and C.G. performed experimental bench work. H.V., J.J.T. and H.S. helped design temperature-control devices. B.D.K., M.T. and K.C.H. analysed the data. B.D.K., L.W. and K.C.H. developed the TSEN model. J.R. contributed strains. H.S., J.E.E. and K.C.H. supervised the research. B.D.K. and K.C.H. wrote the manuscript with input from all authors.

Competing interests

The authors declare no competing interests.

Additional information

Extended data is available for this paper at https://doi.org/10.1038/s41564-024-01841-4.

Supplementary information The online version contains supplementary material available at https://doi.org/10.1038/s41564-024-01841-4.

Correspondence and requests for materials should be addressed to Kerwyn Casey Huang.

Peer review information *Nature Microbiology* thanks the anonymous reviewers for their contribution to the peer review of this work.

https://doi.org/10.1038/s41564-024-01841-4

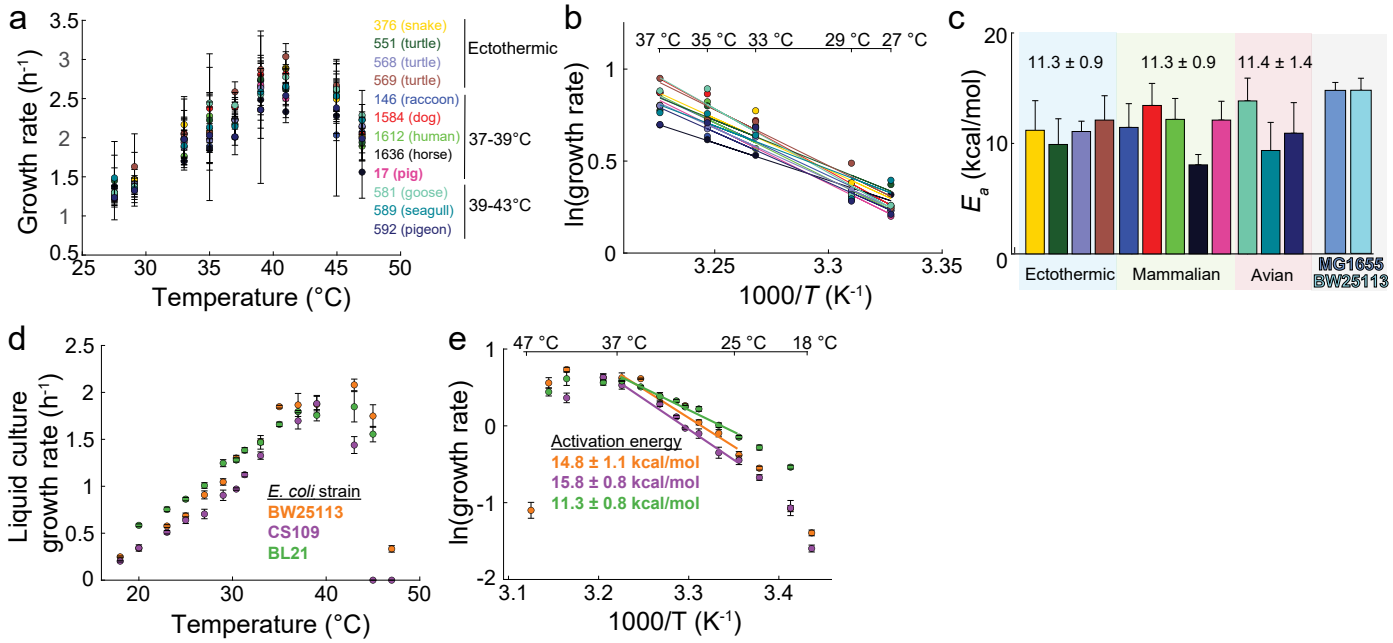

Extended Data Fig. 1 | *E. coli* exhibits robust Arrhenius behavior with a highly conserved activation energy. a) Liquid-culture maximal growth rates across temperatures of diverse *E. coli* strains from various animal hosts (Methods). Each strain is labeled with its laboratory accession number (Supplementary Table 1), host source, and estimated host body temperature. Each data point represents the mean of eight biological replicates, with error bars representing the standard deviation. **b**) Arrhenius plots of growth rates from (**a**). The natural logarithm of maximal growth rate is plotted against the inverse absolute temperature for temperatures between 27 °C and 37 °C, along with weighted linear fits for each strain. **c**) Activation energies measured as the slope of the linear fit to the data in (**b**) for each *E. coli* strain, with errors reported as the standard error of the mean (SEM) from the weighted fit. Each strain is grouped according to host body temperature (blue: Ectothermic, green: Mammalian, red: Avian, gray: Laboratory (MG1655, BW25113)). Each bar represents the mean of eight biological replicates. **d**) Steady-state maximum growth rates in rich medium (LB) of *E. coli* BW25113, CS109, and BL21 between 18 °C and 47 °C (Methods). Each maximal growth rate is reported as the mean±1 standard deviation of eight biological replicates. **e**) Arrhenius plot of growth rates from (**d**). The natural logarithm of maximal growth rate is plotted against the inverse absolute temperature. Growth rates measured at temperatures between 25 °C and 37 °C were used for measuring the activation energy (slope, E_a).

https://doi.org/10.1038/s41564-024-01841-4

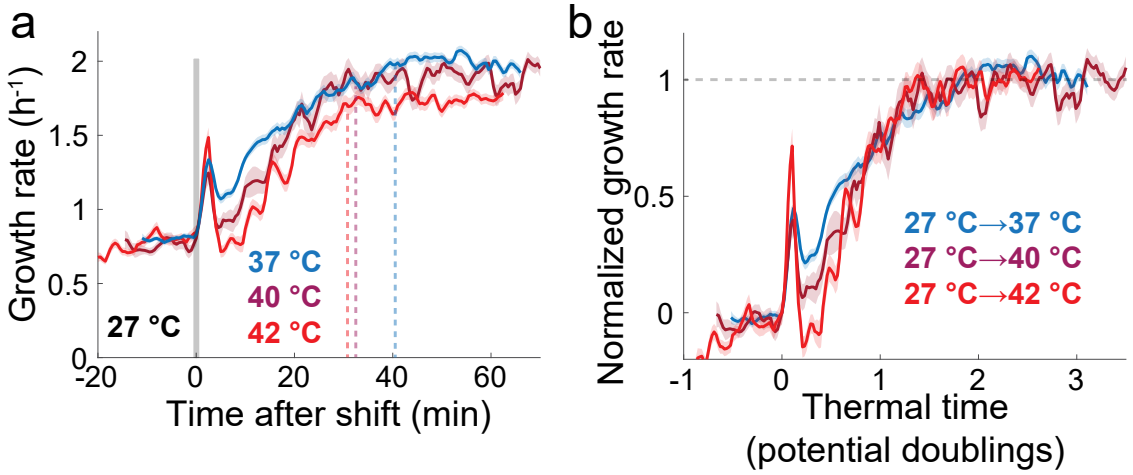

Extended Data Fig. 2 | Temperature upshifts to mild heat-shock temperatures are characterized by slower final growth rates but similar normalized response times. a) Single-cell growth rates of *E. coli* MG1655 on rich medium (LB) undergoing temperature upshifts from 27 °C to 37 °C (blue, *n*=792 cells), 40 °C (purple, *n*=278 cells), or 42 °C (red, *n*=474 cells). Data are the mean±1 SEM (shaded region) at each time point. **b**) Normalized growth rate versus thermal time follows a common trajectory for each upshift in (**a**).

https://doi.org/10.1038/s41564-024-01841-4

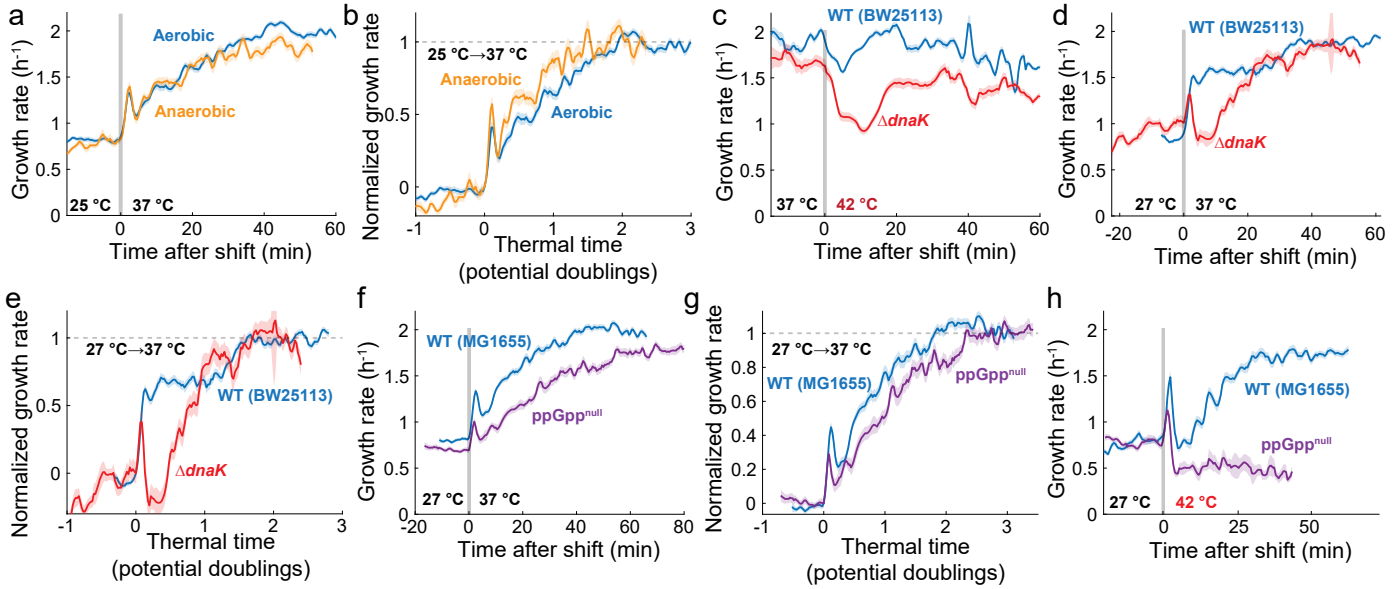

Extended Data Fig. 3 | Effect of chaperones, oxygen, and the stringent response on temperature upshift responses. a) Single-cell growth rates of *E. coli* MG1655 on rich medium (LB) undergoing a temperature upshift from 25 °C to 37 °C in aerobic (blue, *n*=773 cells) or anaerobic (orange, *n*=319 cells) conditions. Data are the mean±1 SEM (shaded region) at each time point. **b**) Normalized growth rate versus thermal time for each trajectory in (**a**). **c**) Single-cell growth rates of Δ*dnaK* (red, *n*=433 cells) and its parent BW25113 (blue, *n*=1011 cells) on rich medium (LB) undergoing a temperature upshift from 37 °C to 42 °C. Data are the mean±1 SEM (shaded region) at each time point. **d**) Single-cell growth rates of Δ*dnaK* (red, *n*=318 cells) and its parent BW25113 (blue, *n*=734 cells) on rich medium (LB) undergoing a temperature upshift from 27 °C to 37 °C. Data are the mean±1 SEM (shaded region) at each time point. **e**) Normalized growth rate versus thermal time for each trajectory in (**d**). **f**) Single-cell growth rates of a ppGpp^{null} strain (Δ*relA* Δ*spoT*) (purple, *n*=648 cells) and its parent MG1655 (blue, *n*=792 cells) on rich medium (LB) undergoing a temperature upshift from 27 °C to 37 °C. Data are the mean±1 SEM (shaded region) at each time point. **g**) Normalized growth rate versus thermal time for each trajectory in (**f**). **h**) Single-cell growth rates of ppGpp^{null} (purple, *n*=47 cells) and its parent MG1655 (blue, *n*=474 cells) on rich medium (LB) undergoing a temperature upshift from 27 °C to 42 °C. Data are the mean±1 SEM (shaded region) at each time point.

https://doi.org/10.1038/s41564-024-01841-4

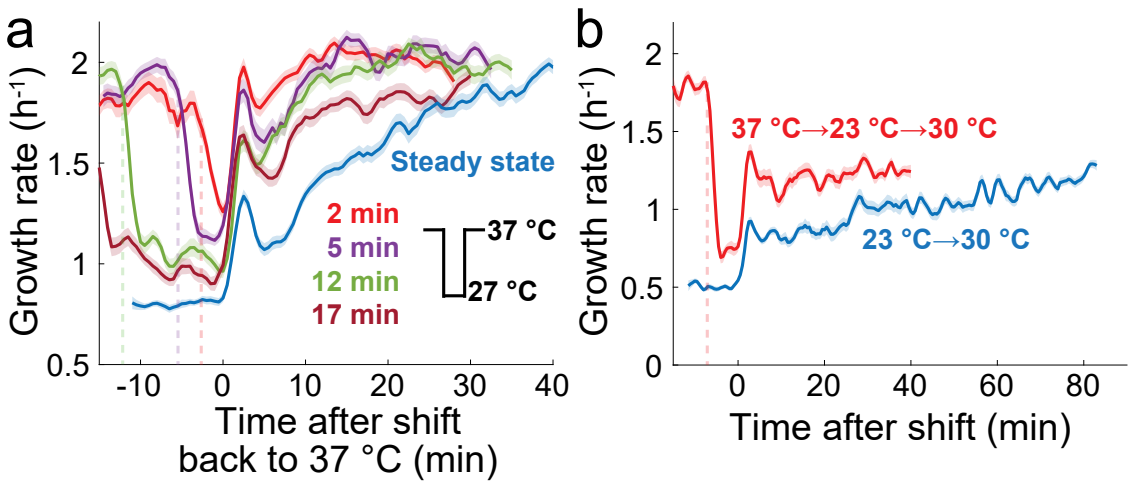

Extended Data Fig. 4 | Downshift pulses reveal temperature history. a) Single-cell growth rates of *E. coli* MG1655 on rich medium (LB) starting at 37 °C subjected to 27 °C pulses for 2 min (red, *n*=519 cells), 5 min (purple, *n*=397 cells), 12 min (green, *n*=451 cells), or 17 min (dark red, *n*=422 cells). Dotted lines represent the time at which cells were subjected to a 27 °C downshift. The shift from steady-state growth at 27 °C to 37 °C is also shown for comparison (blue, *n*=773 cells). Data are the mean±1 SEM (shaded region). **b**) Single-cell growth rates of *E. coli* MG1655 on rich medium (LB) starting at 37 °C subjected to a 23 °C pulse for 5 min before an upshift to the intermediate temperature 30 °C (red, *n*=330 cells). The vertical dashed line indicates the start of cooling, which required ~2 min to reach 23 °C. The shift from steady-state growth at 23 °C to 30 °C is also shown for comparison (blue, *n*=396 cells).

https://doi.org/10.1038/s41564-024-01841-4

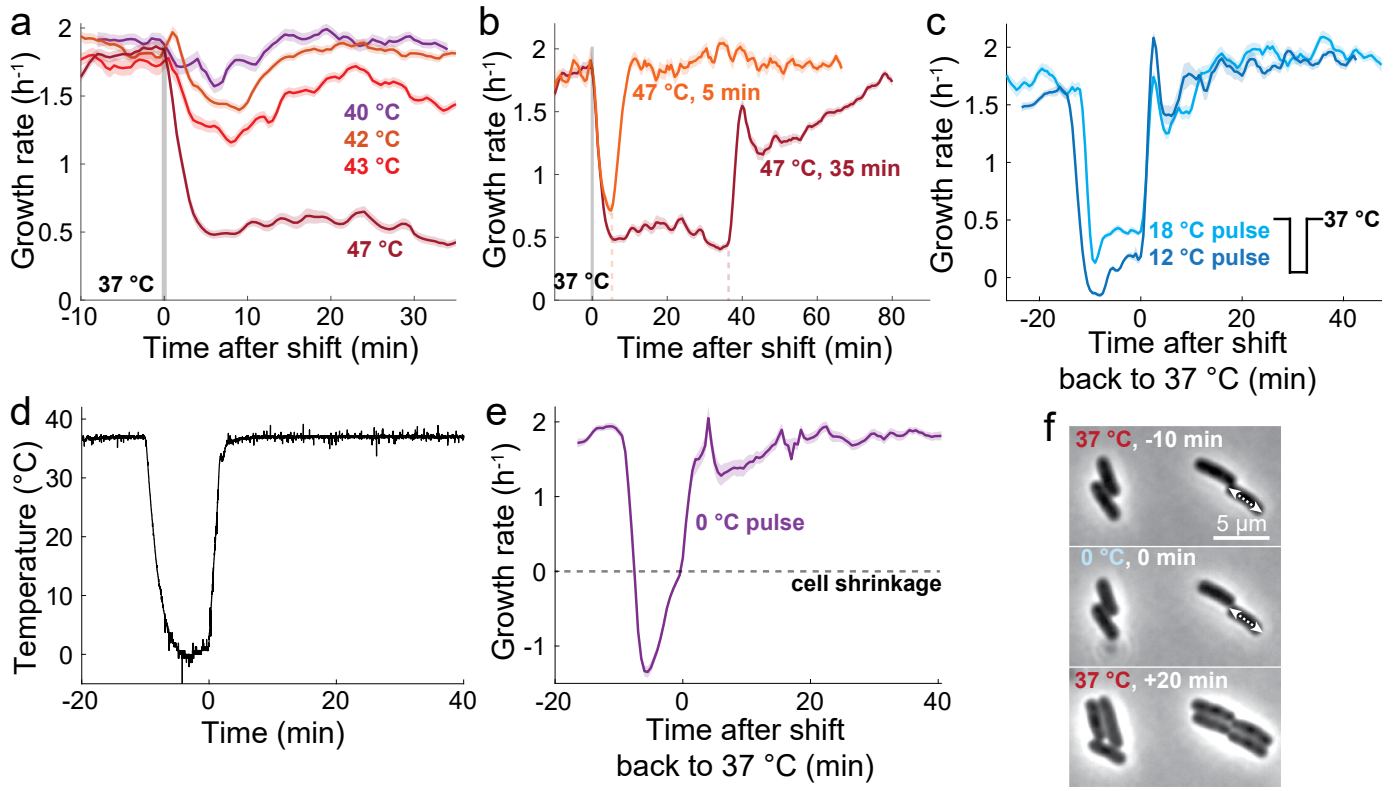

Extended Data Fig. 5 | *E. coli* growth rate responds rapidly to heat-shock and cold-shock pulses. a) Single-cell growth rates of *E. coli* MG1655 on rich medium (LB) undergoing temperature upshifts from 37 °C to 40 °C (purple, n=479 cells), 42 °C (orange, n=1249 cells), 43 °C (red, n=819 cells), or 47 °C (dark red, n=474 cells). Data are the mean±1 SEM (shaded region) at each time point. **b**) Single-cell growth rates of *E. coli* MG1655 on rich medium (LB) starting at 37 °C and subjected to heat-shock pulses at 47 °C for 5 min (orange, n=381 cells) or 35 min (dark red, n=474 cells). Vertical dashed lines represent the times at which cells were shifted back to 37 °C. Data are the mean±1 SEM (shaded region) at each time point. **c**) Single-cell growth rates of *E. coli* MG1655 on rich medium (LB) starting at 37 °C and subjected to ~10-min cold-shock pulses at 18 °C (light blue, n=361 cells) or 12 °C (dark blue, n=390 cells). Data are the mean±1 SEM (shaded region) at each time point. **d**) Temperature readout of a 5-min pulse at 0 °C (Methods) starting from 37 °C. t=0 is when cells were shifted back to 37 °C. **e**) Single-cell growth rates of *E. coli* MG1655 on rich medium (LB) starting at 37 °C and subjected to a 5-min cold-shock pulse at 0 °C (purple, n=283 cells) shown in (**d**). Horizontal dashed line represents cell shrinkage defined as growth rate <0 h^{-1}. Data are the mean±1 SEM (shaded region) at each time point. **f**) Images of *E. coli* MG1655 on rich medium (LB) during a 10-min pulse at 0 °C starting from 37 °C. At 37 °C, cells exhibited normal morphologies and growth (top). At 0 °C, cells shrank, as exemplified by the cell whose length at t=-10 min represented by a double-arrowed line extends beyond the cell boundary at t=0 (middle). Growth resumed quickly after the sample was heated back to 37 °C, without loss in cell viability (bottom).

https://doi.org/10.1038/s41564-024-01841-4

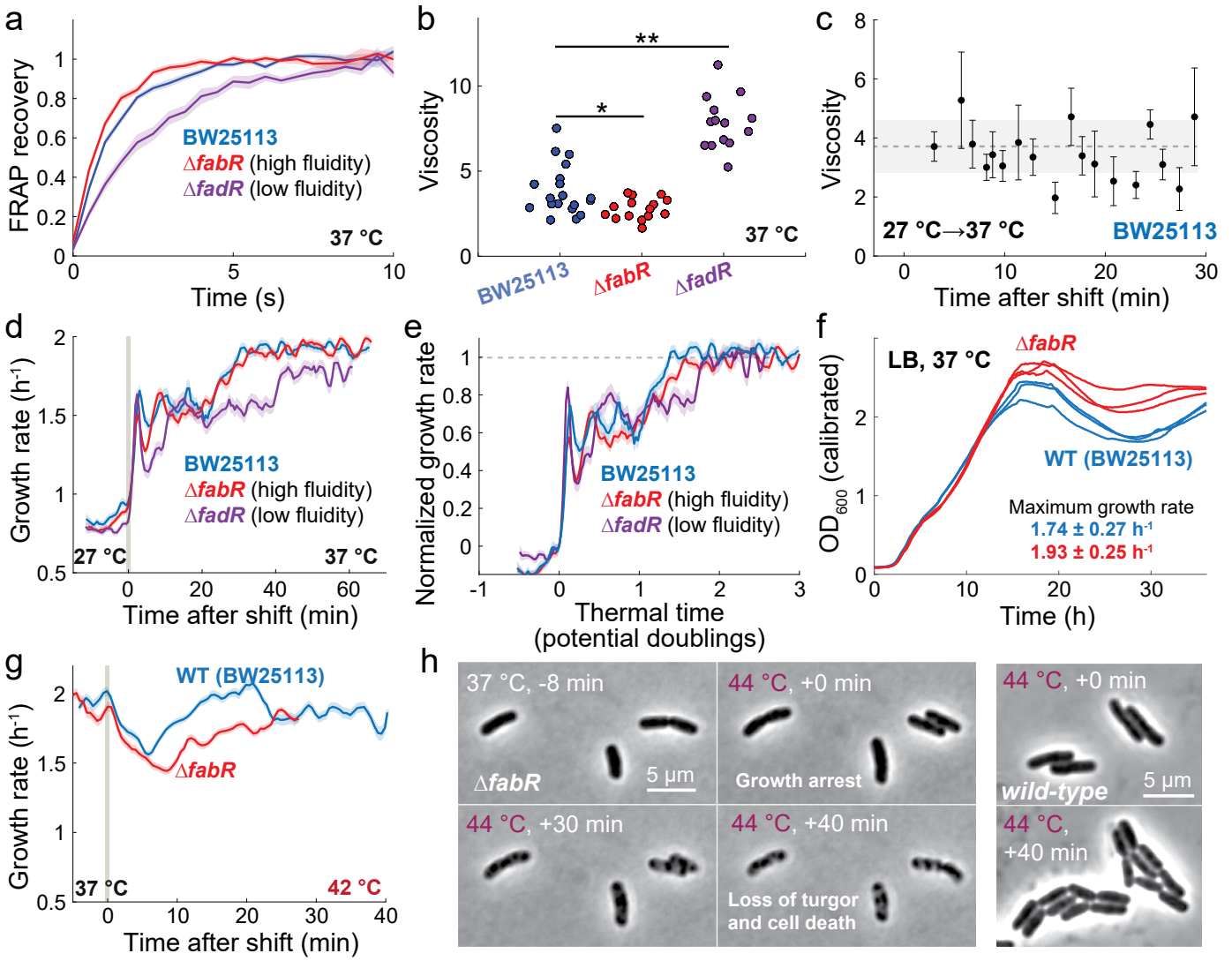

Extended Data Fig. 6 | Changes in membrane fluidity do not alter the response to temperature upshift but increase lysis at high temperatures. a) FRAP recovery dynamics of the membrane dye MitoTracker in the parent strain BW25113 (blue, n=19 cells), the high-fluidity mutant Δ*fabR* (red, n=15 cells), and the low-fluidity mutant Δ*fadR* (purple, n=14 cells) grown on LB (Methods). Curves show the mean recovery and shaded regions represent ±1 SEM. **b**) Membrane viscosity (Methods) was significantly lower and higher in Δ*fabR* and Δ*fadR*, respectively, compared with the parent. Significance was determined using a two-sample t-test (two-sided); *: p=0.013, **: $p<1.8\times10^{-8}$. **c**) Membrane viscosity of *E. coli* BW25113 cells after an upshift at t=0 from 27 °C to 37 °C in LB (Methods). Points are estimates from a best fit (Methods) and error bars represent 1 standard error. Dotted line is the mean viscosity from steady-state measurements (**b**), and the shaded region represents ±1 standard deviation. **d**) Growth rate responses of *E. coli* BW25113 (blue, n=686 cells), Δ*fabR* (red, n=924 cells), and Δ*fadR* (purple, n=409 cells) to a temperature upshift from 27 °C to 37 °C in LB. Curves show mean growth rate and shaded regions represent ±1 SEM. **e**) Normalized growth rate followed a similar trajectory versus thermal time among the mutants and parent for the data in (**d**). **f**) Growth curves of wild-type (BW25113) (blue) and Δ*fabR* (red) cells grown in LB at 37 °C (n=3 replicates). Optical density (OD) was corrected for non-linearity at high OD values (Methods). Maximum growth rates are the mean across replicates and the error is ±1 standard deviation. **g**) Growth rate response to a temperature upshift from 37 °C to 42 °C in *E. coli* BW25113 (blue, n=1011 cells) and Δ*fabR* (red, n=554 cells). Both strains exhibited an initial decrease in growth rate followed by recovery to the steady-state growth rate at 37 °C, but recovery was more delayed for the high-fluidity Δ*fabR* mutant. Curves show mean growth rate and shaded regions represent ±1 SEM. **h**) (Left) Representative images of Δ*fabR* cells throughout a temperature upshift from 37 °C to 44 °C. At 37 °C, morphology and growth were wild-type-like (top left). Growth halted immediately after the shift to 44 °C (top right), with loss of turgor and cell death occurring within 30–40 min after the shift (bottom left, right). (Right) Representative images of wild-type MG1655 cells before and after an upshift from 37 °C to 44 °C. Cells maintained growth and shape.

https://doi.org/10.1038/s41564-024-01841-4

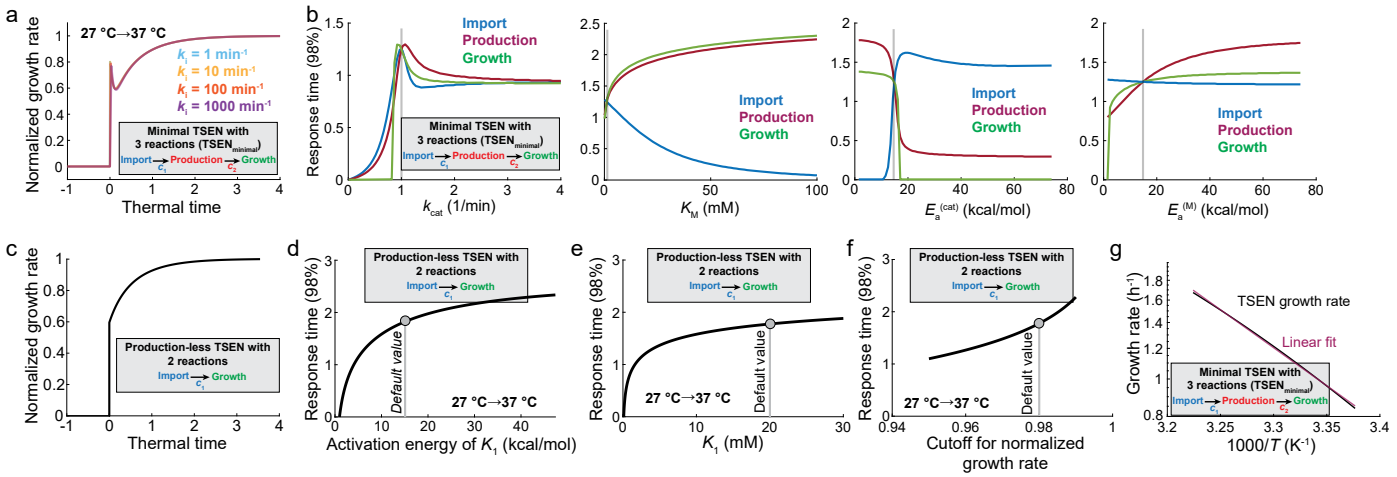

Extended Data Fig. 7 | Effects of changes in TSEN model parameters on temperature-shift response dynamics. a) Increasing the catalytic rate (k_i) for each reaction in a bottlenecked minimal TSEN model (gray box) from 1 min^{-1} to 1000 min^{-1} has virtually no effect on the response. **b**) Effect of model parameters on the normalized response time to a temperature upshift from 27 °C to 37 °C in the minimal TSEN model (gray box) for each reaction (import, production, growth). The definitions of each parameter are provided in Fig. 4a. All other parameters were set to default values (vertical gray bars) in each simulation. Notably, increases in the activation energy of the K_M of the production reaction produced the largest increase in response times across all activation energies (right). **c**) The analytically tractable production-less TSEN model (gray box, Supplementary Text) predicts a non-zero response time. The simulation used default parameters (k_i=1 min^{-1}, K_M = 1 mM, E_a^{cat} = 15 kcal/mol, E_a^M=15 kcal/mol), with the exception of the Michaelis-Menten constant of the second reaction K_1=20 mM. **d**) Normalized response time increases with increased activation energy of K_1 in the production-less TSEN model (gray box). **e**) Normalized response time increases with increased K_1 in the production-less TSEN model (gray box). **f**) Normalized response time was between 1 and 2 doublings when the cutoff used to define the adaptation was increased from 95% to 99% of the steady-state growth rate difference in the production-less TSEN model (gray box). **g**) Arrhenius plot of steady-state growth rate across temperatures predicted by the minimal TSEN model (gray box) exhibits slightly non-linear behavior.

https://doi.org/10.1038/s41564-024-01841-4

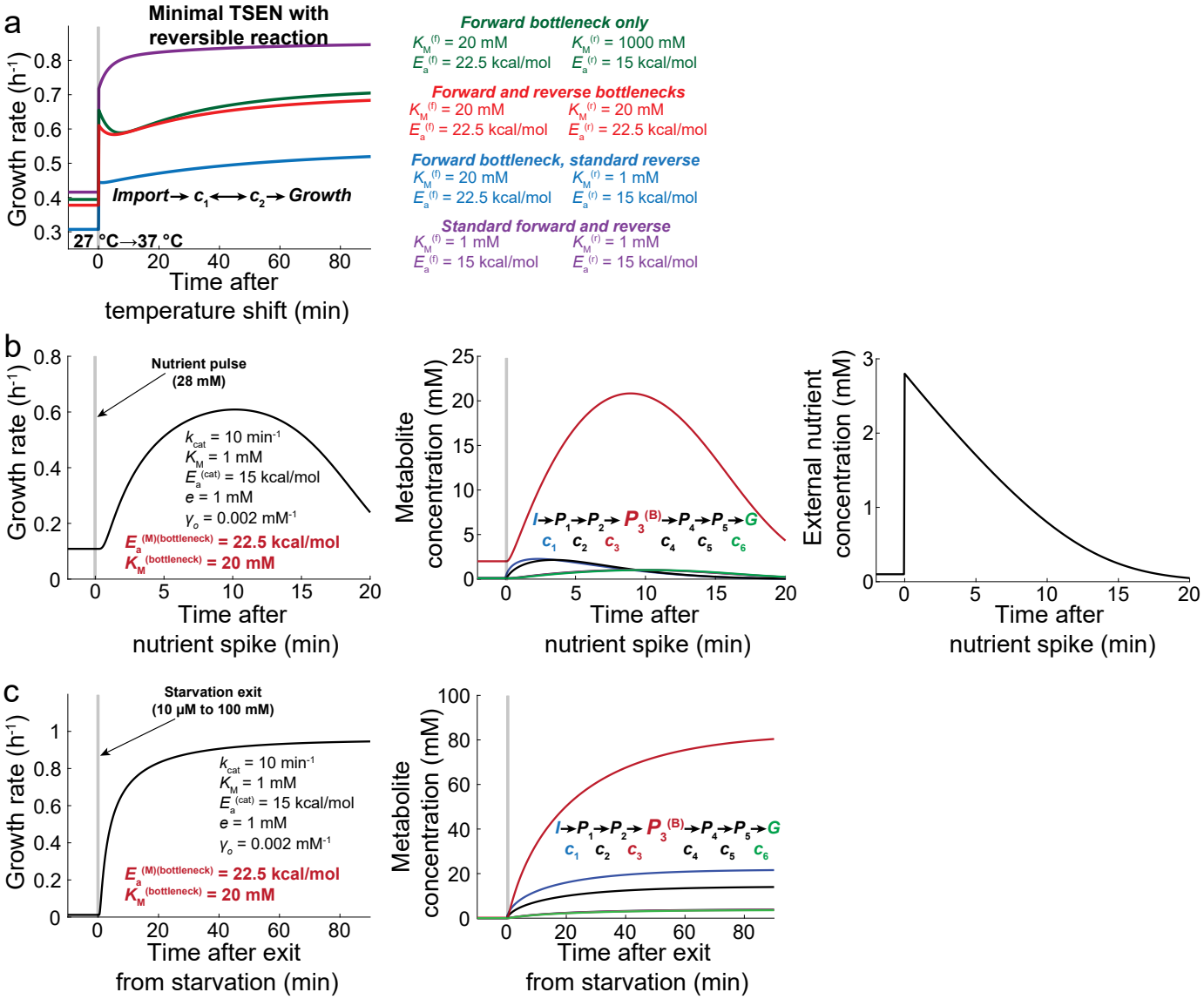

Extended Data Fig. 8 | TSEN model is compatible with reversible enzyme kinetics and predicts nutrient perturbation responses. a) Predictions of the minimal TSEN (3 total reactions, single intermediate) with a reversible intermediate reaction for a temperature upshift from 27 °C to 37 °C (Supplementary Text). Simulations are shown for various values of the Michaelis-Menten constants for the reversible reaction. The standard bottleneck is defined as $K_M = 20$ mM, which has an activation energy of $E_a = 22.5$ kcal/mol. Standard reactions have $K_M = 1$ mM and $E_a = 15$ kcal/mol. Simulations were conducted with saturating external nutrients ($c_0 = 100$ mM). Other parameters of the minimal TSEN can be found in Fig. 4a, b. Green: with a forward bottleneck only, described by a very large reverse $K_M = 1000$ mM. Red: with bottlenecks in both the forward and reverse reactions. Blue: with a forward bottleneck and standard reverse reaction. Purple: with forward and reverse reactions both possessing standard K_M values. **b**) The TSEN model responds to a nutrient pulse from a steady state with low nutrient concentration through increased metabolite production. The full TSEN (5 intermediate reactions) with a single bottleneck (standard kinetic values in black, bottleneck values in red on left) was simulated under sub-saturating, low-nutrient conditions (c_0 =0.1 mM) until steady state was reached, and then an instantaneous nutrient pulse of 28 mM was added at $t = 0$ min, with no nutrients subsequently provided. Simulations were performed in a 1 L container. Left: growth rate dynamics predicted by the bottlenecked TSEN after the nutrient pulse. Standard (black) and bottleneck (red) parameter values are shown. Middle: predicted intracellular metabolite concentrations, colored by location in network during the nutrient pulse and subsequent depletion. Dynamics depend on network position. Right: External nutrient concentration throughout the simulation. **c**) The TSEN model responds to starvation exit through slow metabolite production. The full TSEN (5 intermediate reactions) with a single bottleneck (standard kinetic values in black, bottleneck values in red on left) was simulated under starvation-like conditions (c_0 =0.01 mM) until steady state was reached, and then the nutrient concentration was shifted to a saturating condition (c_0 = 100 mM) at $t = 0$ min. Left: growth rate dynamics after the nutrient shift predicted by the bottlenecked TSEN. Standard (black) and bottleneck (red) parameter values are shown. Right: intracellular metabolite concentrations, colored by position in network, during the shift.

https://doi.org/10.1038/s41564-024-01841-4

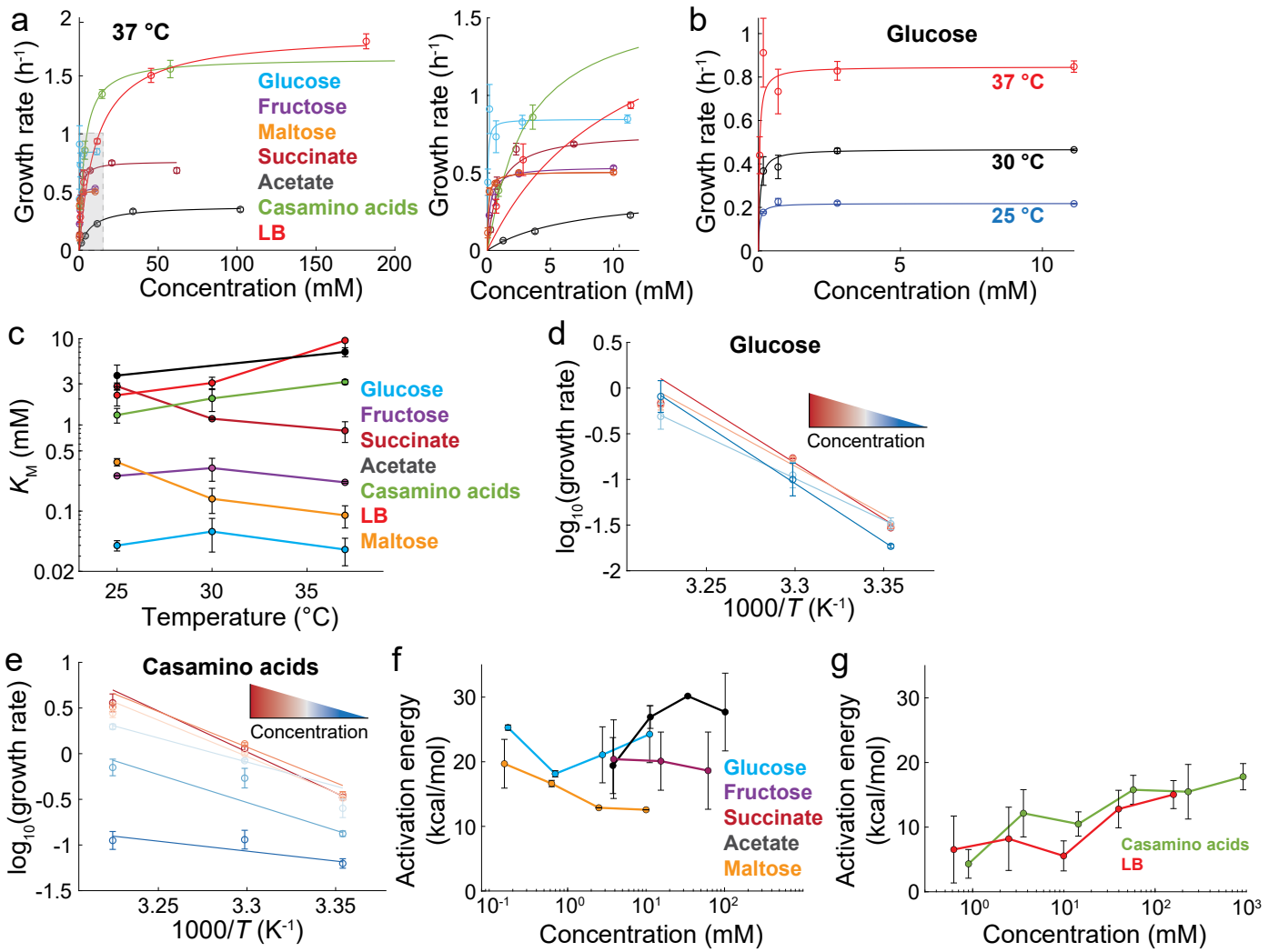

Extended Data Fig. 9 | *E. coli* exhibits Michaelis-Menten kinetics across substrates. a) Left: Liquid-culture growth rates of *E. coli* MG1655 grown on a variety of substrates at 37 °C (Methods). Data are the mean of the maximum growth rate extracted from three biological replicate growth curves and error bars represent ±1 standard deviation (SD). Right: Expanded view of growth rates versus concentration from the outlined box on the left. **b**) Liquid-culture growth rates of *E. coli* MG1655 in MOPS minimal medium supplemented with various concentrations of D-glucose at 25 °C (blue), 30 °C (black), or 37 °C (red). Data are the mean of the maximum growth rate extracted from three biological replicate growth curves and error bars represent ±1 SD. **c**) Michaelis-Menten constants (K_M) of *E. coli* MG1655 grown rates across growth media and temperatures. Data are estimates from a non-linear weighted fit and error bars represent ±1 SEM. **d**) Arrhenius plots of ln(growth rate) versus 1/(absolute temperature) for *E. coli* MG1655 grown in MOPS minimal medium supplemented with glucose at concentrations between 0.17 mM and 11 mM (blue-to-red). Data are the mean across three biological replicates and error bars represent ±1 SD. Weighted linear fits were performed for each concentration. **e**) Arrhenius plots of ln(growth rate) versus 1/(absolute temperature) for *E. coli* MG1655 grown in MOPS minimal medium supplemented with casamino acids at concentrations between 0.9 mM and 923 mM (blue-to-red). Data are the mean across three biological replicates and error bars represent ±1 SD. Weighted linear fits were performed for each concentration. **f**) Activation energy versus substrate concentration of *E. coli* MG1655 grown in minimal media without amino acids supplemented with glucose, fructose, acetate, succinate, or maltose. Activation energies are estimates from a linear weighted fit of Arrhenius plots and error bars represent ±1 SEM. **g**) Activation energy versus substrate concentration of *E. coli* grown in LB (red) or MOPS minimal medium supplemented with casamino acids (green). Activation energies are estimates from a linear weighted fit of Arrhenius plots and error bars represent ±1 SEM.

https://doi.org/10.1038/s41564-024-01841-4

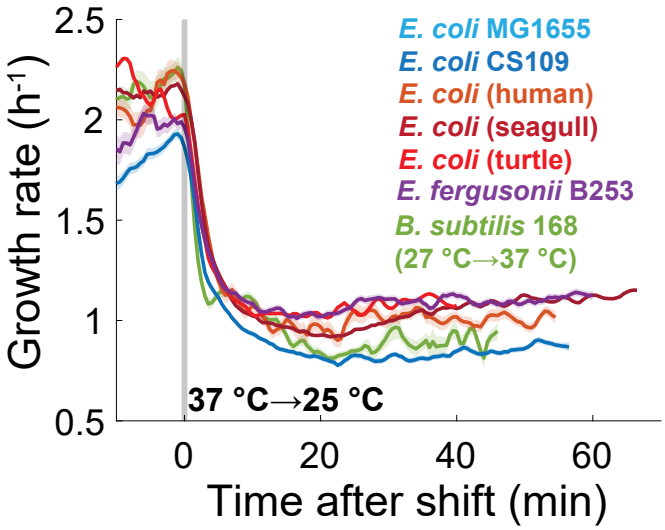

Extended Data Fig. 10 | Growth rate response to a temperature downshift is rapid across organisms. Single-cell growth rate response to a temperature downshift on rich medium (LB) of laboratory-evolved (blue, CS109, *n*=911 cells) and naturally isolated *E. coli* strains (orange to red, *n*=417-1186 cells), *Escherichia fergusonii* (purple, *n*=902 cells), and *Bacillus subtilis* (green, *n*=117 cells). All downshifts were from 37 °C to 25 °C, except for *B. subtilis* (37 °C to 27 °C). Data are the mean±1 SEM (shaded region) at each time point.

nature portfolio

Corresponding author(s): Kerwyn Casey Huang

Last updated by author(s): Aug 11, 2024

Reporting Summary

Nature Portfolio wishes to improve the reproducibility of the work that we publish. This form provides structure for consistency and transparency in reporting. For further information on Nature Portfolio policies, see our Editorial Policies and the Editorial Policy Checklist.

Statistics

For all statistical analyses, confirm that the following items are present in the figure legend, table legend, main text, or Methods section.

n/a	Confirmed	
☐	☒	The exact sample size (*n*) for each experimental group/condition, given as a discrete number and unit of measurement
☐	☒	A statement on whether measurements were taken from distinct samples or whether the same sample was measured repeatedly
☐	☒	The statistical test(s) used AND whether they are one- or two-sided *Only common tests should be described solely by name; describe more complex techniques in the Methods section.*
☐	☒	A description of all covariates tested
☐	☒	A description of any assumptions or corrections, such as tests of normality and adjustment for multiple comparisons
☐	☒	A full description of the statistical parameters including central tendency (e.g. means) or other basic estimates (e.g. regression coefficient) AND variation (e.g. standard deviation) or associated estimates of uncertainty (e.g. confidence intervals)
☐	☒	For null hypothesis testing, the test statistic (e.g. *F*, *t*, *r*) with confidence intervals, effect sizes, degrees of freedom and *P* value noted *Give P values as exact values whenever suitable.*
☒	☐	For Bayesian analysis, information on the choice of priors and Markov chain Monte Carlo settings
☐	☒	For hierarchical and complex designs, identification of the appropriate level for tests and full reporting of outcomes
☐	☒	Estimates of effect sizes (e.g. Cohen's *d*, Pearson's *r*), indicating how they were calculated

Our web collection on statistics for biologists contains articles on many of the points above.

Software and code

Policy information about availability of computer code

Data collection	MicroManager v. 1.4 or Zeiss Zen was used for image acquisition, Processing IDE for temperature data acquisition, BioTek Gen5 for optical density measurements, and LTQ Orbitrap Elite instrument software for mass spectrometry.
Data analysis	MATLAB v2019b and v2022b were used for all custom analysis code, Morphometrics v. 1.1 (MATLAB) for image segmentation, DeepCell (Python v. 3.8.5) for deep-learning image analysis, Proteome Discoverer 2.2.0.388 for mass spectra searching, and R v. 4.0.3 for sequence analysis.

For manuscripts utilizing custom algorithms or software that are central to the research but not yet described in published literature, software must be made available to editors and reviewers. We strongly encourage code deposition in a community repository (e.g. GitHub). See the Nature Portfolio guidelines for submitting code & software for further information.

Data

Policy information about availability of data

All manuscripts must include a data availability statement. This statement should provide the following information, where applicable:

- Accession codes, unique identifiers, or web links for publicly available datasets
- A description of any restrictions on data availability
- For clinical datasets or third party data, please ensure that the statement adheres to our policy

Imaging datasets used for growth rate analyses are available from the corresponding author upon reasonable request. Processed and analyzed imaging datasets of

growth trajectories, liquid growth data, and transposon sequencing data will be made available on the Stanford Digital Repository before publication. Proteomics data will be deposited to the ProteomeXchange Consortium via the PRIDE database before publication.

Research involving human participants, their data, or biological material

Policy information about studies with human participants or human data. See also policy information about sex, gender (identity/presentation), and sexual orientation and race, ethnicity and racism.

Reporting on sex and gender	N/A
Reporting on race, ethnicity, or other socially relevant groupings	N/A
Population characteristics	N/A
Recruitment	N/A
Ethics oversight	N/A

Note that full information on the approval of the study protocol must also be provided in the manuscript.

Field-specific reporting

Please select the one below that is the best fit for your research. If you are not sure, read the appropriate sections before making your selection.

☒ Life sciences ☐ Behavioural & social sciences ☐ Ecological, evolutionary & environmental sciences

For a reference copy of the document with all sections, see nature.com/documents/nr-reporting-summary-flat.pdf

Life sciences study design

All studies must disclose on these points even when the disclosure is negative.

Sample size	In microscopy experiments, sample size is the number of cells. In liquid culture optical density measurements, sample number is the number of growth curve replicates. In both the proteomics experiments and pooled mutant screen, sample size is the number of biological replicates.
Data exclusions	Single cell trajectories were excluded based on cell tracking errors (incorrect cell assignment) and a minimum trajectory length. Peptides and proteins were filtered according to a false discovery rate of 1% (a standard process). In barcode sequencing analysis, reads were excluded if they corresponded to an insertion that was not within the central 10–90% of the coding region (a standard process).
Replication	Replication of wild-type responses to temperature shifts was performed at least twice for each condition. Liquid culture optical density measurements were carried out in replicates of at least 3. Proteomics and pooled mutant screens had 2 biological replicates for each sample. All replications were successful for these experiments. Some single-cell microscopy experiments reported were not replicated, due to either null results or if they comprised a larger trend in the dataset.
Randomization	Control groups in this study were unperturbed cell samples. Cellular populations were divided randomly by mixing before splitting into control and experimental groups.
Blinding	Blinding was not relevant to our study, as clonal cell populations could not be discriminated. Additionally, experiments performed in this study were targeted perturbations, requiring detailed knowledge of the cellular system's growth state, which was monitored frequently.

Reporting for specific materials, systems and methods

We require information from authors about some types of materials, experimental systems and methods used in many studies. Here, indicate whether each material, system or method listed is relevant to your study. If you are not sure if a list item applies to your research, read the appropriate section before selecting a response.

Materials & experimental systems

n/a	Involved in the study
☒	☐ Antibodies
☒	☐ Eukaryotic cell lines
☒	☐ Palaeontology and archaeology
☒	☐ Animals and other organisms
☒	☐ Clinical data
☒	☐ Dual use research of concern
☒	☐ Plants

Methods

n/a	Involved in the study
☒	☐ ChIP-seq
☒	☐ Flow cytometry
☒	☐ MRI-based neuroimaging